



HAL
open science

Eoarchean subduction-like magmatism recorded in 3750 Ma mafic–ultramafic rocks of the Ukaliq supracrustal belt (Québec)

Thomas Grocolas, Pierre Bouilhol, Guillaume Caro, Stephen Mojzsis

► To cite this version:

Thomas Grocolas, Pierre Bouilhol, Guillaume Caro, Stephen Mojzsis. Eoarchean subduction-like magmatism recorded in 3750 Ma mafic–ultramafic rocks of the Ukaliq supracrustal belt (Québec). *Contributions to Mineralogy and Petrology*, 2022, 177 (3), pp.39. 10.1007/s00410-022-01904-x . hal-03608356

HAL Id: hal-03608356

<https://hal.science/hal-03608356>

Submitted on 14 Mar 2022

HAL is a multi-disciplinary open access archive for the deposit and dissemination of scientific research documents, whether they are published or not. The documents may come from teaching and research institutions in France or abroad, or from public or private research centers.

L'archive ouverte pluridisciplinaire **HAL**, est destinée au dépôt et à la diffusion de documents scientifiques de niveau recherche, publiés ou non, émanant des établissements d'enseignement et de recherche français ou étrangers, des laboratoires publics ou privés.



Eoarchean subduction-like magmatism recorded in 3750 Ma mafic–ultramafic rocks of the Ukaliq supracrustal belt (Québec)

Thomas Grocolas^{1,2} · Pierre Bouilhol¹ · Guillaume Caro¹ · Stephen J. Mojzsis^{3,4,5}

Received: 29 June 2021 / Accepted: 24 February 2022
© The Author(s) 2022

Abstract

Our understanding of the nature of crustal formation in the Eoarchean is limited by the scarcity and poor preservation of the oldest rocks and variable and imperfect preservation of protolith magmatic signatures. These limitations hamper our ability to place quantitative constraints on thermomechanical models for early crustal genesis and hence on the operative geodynamic regimes at that time. The recently discovered ca. 3.75 Ga Ukaliq supracrustal enclave (northern Québec) is mainly composed of variably deformed and compositionally diverse serpentinized ultramafic rocks and amphibolitized mafic schists whose metamorphic peak, inferred from phase equilibria modeling, was below 720 °C. Inferred protoliths to the Ukaliq ultramafic rocks include cumulative dunites, pyroxenites, and gabbros, whereas the mafic rocks were probably picrites, basalts, and basaltic andesites. The bulk-rock and mineral chemistry documents the partial preservation of cumulative pyroxenes and probably amphiboles and demonstrates the occurrence of a clinopyroxene-dominated, tholeiitic suite and an orthopyroxene-dominated, boninite-like suite. Together with the presence of negative $\mu^{142}\text{Nd}$ anomalies in the boninitic basalts, two liquid lines of descent are inferred: (i) a damp tholeiitic sequence resulting from the fractionation of a basaltic liquid produced by mantle decompression; and (ii) a boninitic suite documenting the evolution of an initially primitive basaltic andesite liquid produced by flux melting. Petrographic observations, thermodynamic modeling, bulk-rock and mineral chemistry, and ^{142}Nd isotopic compositions identify the Ukaliq supracrustal belt as the remnant of an Eoarchean arc crust produced by the recycling of Hadean crust in a similar way as modern-style subduction.

Keywords Eoarchean magmatism · Ukaliq supracrustal belt · Liquid line of descent · Subduction

Introduction

Plate tectonics has long governed the mode of crust formation and cooling on our planet, including the long-term operation of the geochemical cycles and, hence, the evolution of the atmosphere, hydrosphere, and biosphere in what has been termed “biogeodynamics” (e.g., Stern 2002; Von Huene and Scholl 1991; Zerkle 2018). Within this biogeodynamic framework, subduction zones generate continental crust through partial melting of the mantle wedge, magmatic accretion beneath island arcs, and refinement via additional remelting and density sorting (e.g., Cawood et al. 2013; Hacker et al. 2011; Ringwood 1974; Schmidt and Jagoutz 2017; Taylor and McLennan 1985). The record of Hf isotopes in zircon is interpreted to show that > 70% of crustal growth occurred in the Archean, or before about 2.5 Ga (e.g., Belousova et al. 2010; McCulloch and Bennett 1994). Based mostly on geochemical and mechanical–structural constraints, the prevailing process associated with Archean

Communicated by Timothy L. Grove.

✉ Thomas Grocolas
thomas.grocolas@unil.ch

¹ Université de Lorraine, CNRS, CRPG, 54000 Nancy, France

² Institute of Earth Sciences, University of Lausanne, Géopolis, 1015 Lausanne, Switzerland

³ Origins Research Institute, Research Centre for Astronomy and Earth Sciences, 15–17 Konkoly Thege Miklós Road, Budapest 1121, Hungary

⁴ Department of Lithospheric Research, University of Vienna, UZA2, Althanstraße 14, 1090 Vienna, Austria

⁵ Department of Geological Sciences, University of Colorado, Boulder, CO 80309-0399, USA

crustal growth asserts that continental drift without subduction as we know it molded the Hadean–Archean Earth's crust (e.g., Bédard et al. 2003; Shirey and Richardson 2011). Considering a mantle potential temperature ~ 300 °C greater than that of today, mantle melting ought to have occurred at a greater depth to produce a relatively thick and buoyant crust (Johnson et al. 2014; Korenaga 2006; McKenzie and Bickle 1988; Sleep 2005). Arguably, the thermal and mechanical properties of such thick crust inhibited subduction processes to instead favor emplacement of a long-lived lithosphere susceptible to reworking via what may have been catastrophic vertical transfer events (e.g., Bédard 2006, 2018; Fischer and Gerya 2016a; O'Neill and Debaille 2014; Van Thienen et al. 2004). At odds with these interpretations are recent numerical models showing that subduction can proceed even under the thermal boundary conditions of very thick and buoyant crust (Maunder et al. 2016; Weller et al. 2019), although other models demonstrate that subduction is inhibited even with a mantle 30 °C hotter in the Proterozoic (e.g., Davies 1992). Polat et al. (2002) present petrological and geochemical constraints from Eoarchean rocks that are compatible with subduction initiation at approximately 3.8 Ga. Similarly, the heavy Si isotope signature of tonalites–trondhjemites–granodiorites (TTG), interpreted to reflect a recycled sedimentary component, lends support to the idea that the onset of plate tectonics occurred at the Hadean–Eoarchean transition around 4 Ga ago rather than sometime later (Deng et al. 2019; Trail et al. 2018). Melt inclusions captured in Hadean zircons analyzed by Hopkins et al. (2008, 2010) are also used to argue for plate-boundary processing of crust before 4 Ga. A competing study of silicate and sulfide inclusions captured in ancient diamonds (Shirey and Richardson 2011), as well as recent studies based on O and B isotopic composition of Paleoarchean to Mesoarchean TTG (Smit et al. 2019; Smithies et al. 2021), instead argues in favor of the initiation of plate tectonics after about 3 Ga, whereas studies of ophiolites and high-pressure metamorphic terranes (Stern 2005) suggest that this process only began as recently as Neoproterozoic time. Therefore, the petrogenetic process associated with the crustal growth trajectory of the Archean Earth remains widely debated because of the poor preservation of crustal material from these early times that could provide direct information on the processes involved in crustal genesis. Hence, resolving these conflicting conclusions about Earth's history of plate tectonics requires analysis of the oldest rocks in addition to numerical modeling. However, this approach is only effective if the oldest preserved rocks can be shown to contain petrological and geochemical characteristics that allow for distinguishing between the competing Archean petrogenetic models cited above.

One such early Archean crustal fragment is the $\sim 12,000$ km² Archean Inukjuak domain in the northeast Superior

Province of Québec, Canada (Greer et al. 2020). Briefly, the Eoarchean supracrustal enclaves of the Ukaliq (and nearby Nuvvuagittuq) locality are part of the Innuksuac complex (Simard et al. 2003), an association of scattered and variably deformed supracrustal rafts which range in size from < 1 m to > 1 km and are in turn intruded by granitoid gneisses of the Inukjuak domain. As described by Caro et al. (2017), the Ukaliq rocks comprise a series of mafic schists interpreted to have volcanic protoliths chemically similar to those found in a modern forearc environment such as tholeiitic and boninitic lavas. These are also associated with calc-alkaline andesites, the identification of which challenges the exclusivity of a vertical tectonic model for the entirety of the Archean (e.g., Turner et al. 2014), although a subduction-less hypothesis has also been advocated by Barnes and Van Kranendonk (2014). We wish to emphasize that rocks from the Innuksuac complex display similar geochemical signatures to rocks documented in the 3.81–3.70 Ga Isua supracrustal belt (ISB; southern West Greenland; Szilas et al. 2015 and references therein) as well as in younger Archean complexes (e.g., Cawood et al. 2006). Yet, as opposed to the ISB rocks which have well documented higher $^{142}\text{Nd}/^{144}\text{Nd}$ values (Caro et al. 2003) relative to bulk silicate Earth (BSE) and reported in the conventional $\mu^{142}\text{Nd}$ notation as positive anomalies, the numerous lithologies of the Innuksuac complex preserve variably negative $\mu^{142}\text{Nd}$ anomalies (Caro et al. 2017; O'Neil et al. 2008; Roth et al. 2013). Because of the short half-life of ^{146}Sm ($t_{1/2} = 103$ Ma), such negative ^{142}Nd anomalies can only be produced in low Sm/Nd (crustal) protoliths differentiated prior to ~ 4 Ga (e.g., Caro 2011).

There are two ways to explain these divergent $\mu^{142}\text{Nd}$ values for what otherwise appears to be synchronous Eoarchean terranes: (i) the negative $\mu^{142}\text{Nd}$ were produced by in situ decay of ^{146}Sm after emplacement of the rocks, in which case the Nuvvuagittuq belt is of Hadean age (O'Neil et al. 2008, 2019); or (ii) the negative $\mu^{142}\text{Nd}$ signature is inherited from a now-vanished Hadean lithosphere and the $\mu^{142}\text{Nd}$ –Sm/Nd correlation interpreted by O'Neil et al. (2008) as an isochron instead represents a mixing line without geochronological significance (Caro et al. 2017; Guitreau et al. 2013). Such an inherited signal can be duplicated by assimilation of a Hadean ^{142}Nd anomaly-bearing crust or foundering of Hadean lithosphere leading to the transfer of a crustal isotopic signature to the overlying mantle wedge.

Two key observations can, however, weaken the assimilation argument. The first of these is that, despite the ubiquitous Hadean crustal signatures, there are no inherited or detrital zircons of Hadean age in rocks of the Innuksuac complex. This is despite thousands of U–Pb zircon analyses performed on samples of igneous and detrital sedimentary protoliths collected from throughout the terrane (Cates et al. 2013; Chowdhury et al. 2020; Greer et al. 2020 and references therein). A second argument

lies in the absence of crustal (felsic) contaminants with sufficiently unradiogenic ^{142}Nd signature to account for the $\mu^{142}\text{Nd}$ values found in mafic rocks of the Nuvvuagittuq and Ukaliq supracrustal belts (Caro et al. 2017). Collectively, these observations suggest that the Innuksuac complex inherited the geochemical signature of Earth's primordial crust without significant reworking of Hadean felsic protoliths. To account for these observations, which appear to conflict with the assimilation scenario to explain the variably negative $\mu^{142}\text{Nd}$ anomalies, we propose that crustal recycling through subduction was operative, at least intermittently, in the Eoarchean. We further show how this scenario neatly explains the typical forearc sequence preserved in the Innuksuac supracrustals and the trace element concentrations and the enriched ^{142}Nd and ^{143}Nd signatures contained therein.

In this work, we focus our attention on the ultramafic–mafic supracrustal enclave at the Ukaliq locality to describe (1) preserved Eoarchean magmatic features, (2) the cumulate–liquid relationship between the ultramafic and mafic rocks, and (3) the cumulate assemblages that formed during the ascent of differentiating magmas. Based on these observations, we provide an explanation for the chemical evolution of the supracrustal rocks that requires a transition from a damp tholeiitic regime to a wet boninitic sequence. In a modern tectonic setting, such an evolution is most often observed in subduction initiation environments.

Geological setting

The variably deformed Eoarchean supracrustal enclaves of the dominantly Neoproterozoic Inukjuak domain (Minto block, northeast Superior Province, Canada) principally comprise plutonic and volcano-sedimentary schists; these range in age from 3.8 to 3.5 Ga and were metamorphosed at amphibolite facies conditions (0.4 GPa, 640 °C; Cates and Mojzsis 2009; Greer et al. 2020) with local retrogressions. Although less well known than cognate Eoarchean rocks of the ISB, the ca. 3.75 Ga Nuvvuagittuq supracrustal belt (NSB) was the first to show evidence of anomalous depletions in $^{142}\text{Nd}/^{144}\text{Nd}$ relative to BSE (negative $\mu^{142}\text{Nd}$) that seem to correlate to Sm/Nd (O'Neil et al. 2008). The subject of our study is another neighboring body of metamorphosed volcano-sedimentary rocks also displaying this characteristic ^{142}Nd signature: the Ukaliq supracrustal belt (USB; Caro et al. 2017). The largest USB enclave is a poly-metamorphosed and intensely deformed NNW-trending flat, ellipsoidal body of about 100 m × 7 km (Fig. 1) a few kilometers north from the NSB. The USB is composed of three main lithologies: (i) a massive amphibolite composed of hornblende- or cummingtonite-rich rocks inferred to have volcanic protoliths; (ii) ultramafic boudins and enclaves, mainly serpentinized; and (iii) intercalated siliceous units comprising layered and strongly tectonized quartz + magnetite ± amphibole ± pyroxene ± olivine rocks interpreted as banded-iron formations (BIF), and quartz + biotite schists and massive to banded

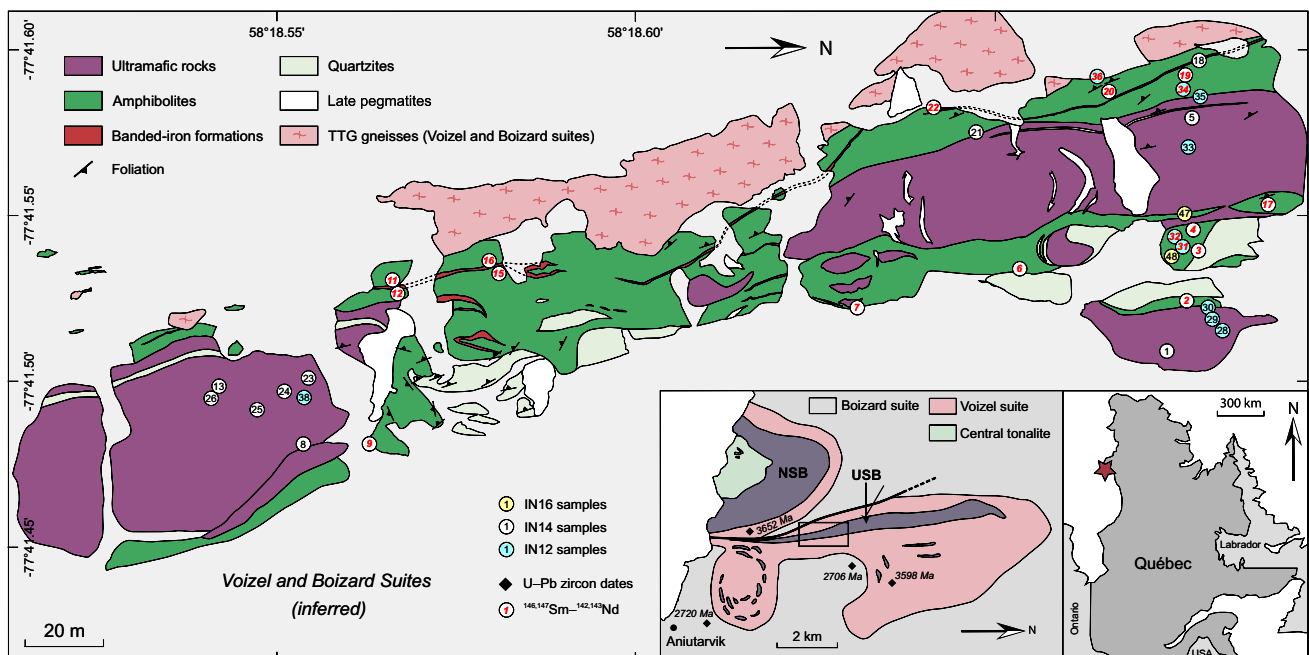


Fig. 1 Geological map of the southernmost Ukaliq supracrustal belt and sample location. Samples analyzed for $^{146,147}\text{Sm}$ – $^{142,143}\text{Nd}$ are from Caro et al. (2017) and U–Pb ages for the Voizel and Boizard suites are from Greer et al. (2020). Modified after Caro et al. (2017)

quartzite (\pm fuchsite) of detrital origin (Caro et al. 2017; Greer et al. 2020).

Two forms of ultramafic rocks can be distinguished: (i) a thick layer (\sim 30 m) parallel to the massive NNW-dipping foliation; and (ii) lenses (1–5 m) included within the amphibolites (Fig. 2a). The contact between ultramafic and mafic rocks is sharp (Fig. 2b) and concordant with the foliation. Several thin (\sim 10 cm) BIF layers occur within the mafic rocks and are parallel to the regional structural trend of the USB enclave. The quartzites are mainly located near the eastern contact between USB rocks and the Voizel suite granitoids (3550 Ma; Greer et al. 2020; Fig. 1). Ultramafic rocks range from pure serpentinite on the eastern side to a more pyroxene-rich composition in the west. The NSB differs from the USB in the occurrence of the Ca-poor amphibole cummingtonite; this lithology is rare at Ukaliq, where the amphibole is hornblende as opposed to the NSB where cummingtonite can be the dominant amphibole in amphibolite. Earlier U–Pb thermal ionization mass spectrometry (TIMS) geochronology on detrital zircons recovered from micaschists in the NSB yields an age of 3825 ± 18 Ma (Darling et al. 2013; David et al. 2002), whereas zircons

extracted from intrusive trondhjemitic orthogneisses lead to a minimum emplacement age of 3751 ± 10 Ma (Cates and Mojzsis 2007; Greer et al. 2020). Elsewhere in the NSB, detrital zircons from detrital fuchsitic quartzites and micaschists interpreted to be quartz-pebble conglomerates provide a maximum age of emplacement for the various volcanic protoliths of ca. 3.78 Ga (Cates et al. 2013; Darling et al. 2013). For a review of the geology of the wider region and a debate over the interpretation of the geochronology, we refer the reader to the synthesis provided in Greer et al. (2020).

Methods

This study uses 35 samples from Caro et al. (2017) and 22 collected in the USB in 2016. The latter were cut into small blocks and only fresh material was further used for bulk-rock analysis. The blocks were crushed in a hydraulic press and ground to a fine powder in an agate mill. Bulk-rock major and trace element compositions for the 22 samples were performed at the Service d'Analyse des Roches et des

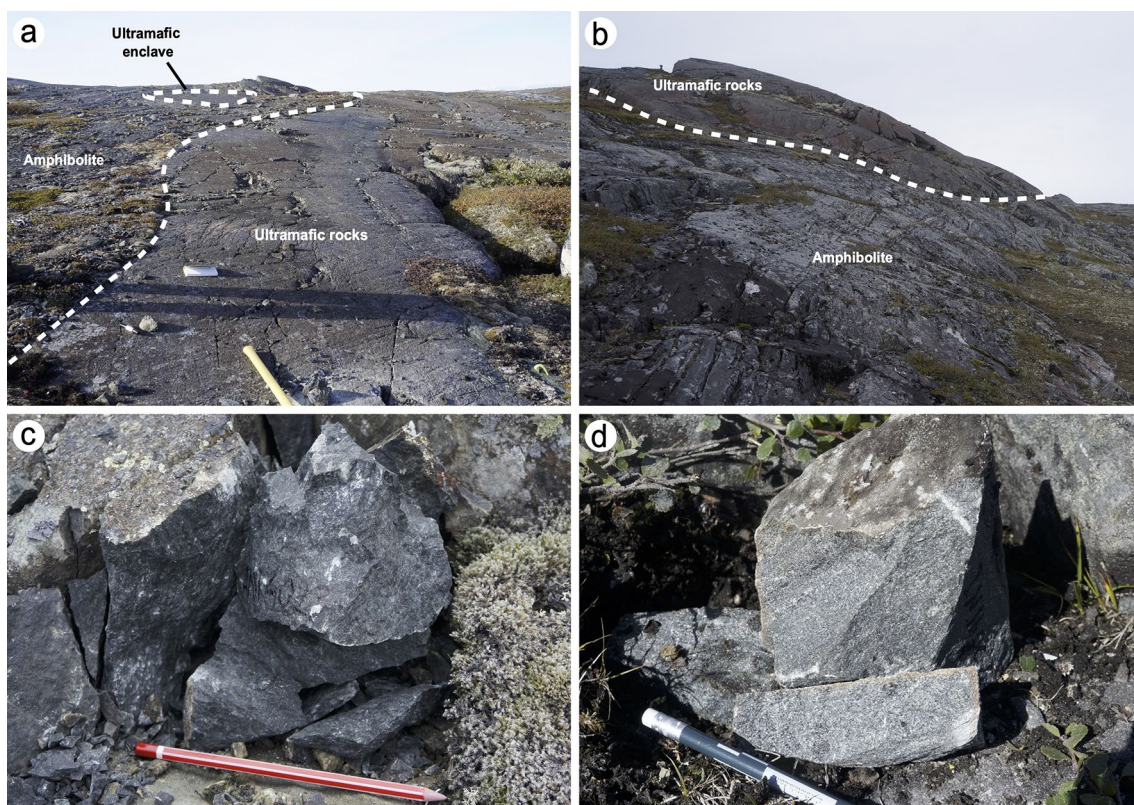


Fig. 2 Ultramafic and mafic rock associations within the Ukaliq supracrustal belt. **a** Ultramafic rocks and amphibolites exhibiting a subvertical contact and an enclave relationship (N58°18.542', W77°41.487'). **b** Sharp contact between amphibolite and ultramafic rocks showing an orange to brownish alteration color. **c** Serpentinitized

ultramafic rock sample (IN14023) displaying a dark greenish color and composed of antigorite + chlorite + magnetite (N58°18.559', W77°41.490'). **d** Photograph of the fine-grained amphibolite exhibiting the typical amph + plag + quartz paragenesis (IN14004; N58°18.682', W77°41.547')

Minéraux (SARM, CRPG) facility using the inductively coupled plasma optical emission spectrometer (ICP-OES) iCap6500 and the inductively coupled plasma mass spectrometer (ICP-MS) iCapQ, respectively. The detection limits and standard deviations are reported in the Electronic Supplementary Material ESM 1.

In situ major element compositions of minerals from a subset of 16 samples (8 ultramafic rocks and 8 amphibolites) were determined using the Cameca SX100 electron microprobe at GeoRessources laboratory (Université de Lorraine). Measurements were corrected with the PRZF method (Armstrong 1995). The acceleration voltage was 15 keV and beam current 12 nA. Counting times were 30 s on the peak and 15 s on the background. Trace element analyses were also performed for 6 samples using an Agilent 7500 sector field ICP-MS coupled with a Geolas platform hosting a 193 nm excimer laser housed at GeoRessources laboratory. Prior to the session, the instrument was tuned in linear scan mode on SRM-612 silicate glass. Oxide generation was mitigated to be < 0.07% for $^{248}\text{ThO}^+ / ^{232}\text{Th}^+$. SRM-612 was also measured during the analytical session twice every 16 analyses to correct for instrumental drift. A 10 Hz repetition rate was used for sample analysis, and laser output energy density was 6 J cm^{-2} . The ablation spot size was 60–80 μm for clinopyroxenes (cpx) and amphiboles (amph), and 120–150 μm for orthopyroxenes (opx). The acquisition time for background was 80 s and laser ablation 35 s. The raw data were processed and transformed into elemental contents using the LAMTRACE software (Jackson 2008). The detection limits and standard deviations are reported in the Electronic Supplementary Material ESM 1.

Structure and petrography

Three main lithologies were identified within the main USB body (see Caro et al. 2017): (i) ultramafic rocks (pyroxenrich to pure serpentinite) present as enclaves or as decimeter-sized layers; (ii) hornblende- or cummingtonite-bearing amphibolites; and (iii) quartzitic and micaceous rocks of sedimentary protolith with foliation parallel to that expressed in the amphibolites. Therefore, contacts between these lithologies are transposed as the foliation never transects layer contacts, even in highly folded areas, such as the southeastern contact between quartzites and amphibolites (Fig. 1).

Ultramafic rocks

The dark green serpentine-bearing ultramafic rocks (Fig. 2c) are located in the center of the Ukaliq supracrustal belt and display an average foliation striking $\text{N}70^\circ \pm 10^\circ$ (Fig. 1). These serpentinites are mainly composed of antigorite and chlorite, as well as magnetite in the groundmass. At the

microscopic scale, a cpx-bearing series and a cpx-absent, opx-bearing series are identified. Only one ultramafic sample is composed of cpx (IN16098b); it is located in a single, separate ultramafic lens and contains > 90 area% of antigorite and chlorite. This sample contains limited amounts (< 1 area%) of submillimeter-sized, fractured cpx in inclusion within magnesio-hornblende (Mg-hbl) or in the antigorite + chlorite groundmass (Fig. 3d). These anhedral Mg-hbl form millimeter-sized porphyroblasts preferentially altered along their cleavage planes, separating them into several subgrains. They are systematically surrounded by a tremolite rim typical of disequilibrium between serpentine and amphibole. Magnetite is ubiquitous in the cpx-bearing ultramafic rock and is in equilibrium with antigorite and chlorite.

The cpx-absent ultramafic rocks are also dominated by the antigorite + chlorite + magnetite + tremolite paragenesis, but centimeter-sized plates of subhedral to euhedral opx may represent > 60 area% of a thin section. These opx can be in contact with or surrounded by Mg-hbl (Fig. 3b), surrounded by antigorite and chlorite (Fig. 3c), or completely transformed into serpentine (Fig. 3a). Antigorite pseudomorph lamellae following opx cleavage can occur and separate opx into several, optically continuous subgrains originally forming large, centimeter-sized opx (Fig. 3c). We interpret these large, partially altered opx as the remnants of an altered cumulative texture (Campbell 1968), while opx-associated antigorite probably forms through fluid circulation along cleavage planes. The Mg-hbl from these samples are similar to those described in the cpx-bearing ultramafic rock. In these cpx-absent ultramafic samples, dark, subhedral to euhedral spinels (spl) occur as inclusion within opx and hbl (Fig. 3b), reminiscent of a typical magmatic relationship (e.g., Bouilhol et al. 2015). Brownish to greenish hercynitic spl are only present in cpx-absent samples and are locally surrounded by magnetite (Fig. 3c), which is typical of disequilibrium between hercynite and serpentine. Finally, talc is locally observed overgrowing antigorite.

Amphibolites

Volumetrically, the USB is dominated by a dark, massive unit and many other smaller deformed enclaves of amphibolites and paragneisses scattered throughout the complex (Chowdhury et al. 2020; Greer et al. 2020). At the centimeter scale, the mafic rocks display a fine-grained (< 0.5 mm) texture (Fig. 2d) with a typically metamorphic amph + plagioclase (plag) + quartz \pm cpx paragenesis. Light gray to beige amphibolite corresponds to the cummingtonite-rich amphibolite much more widespread throughout the neighboring NSB (David et al. 2002). The typical feature of these cummingtonite-bearing amphibolites is the absence of cpx; they will be hereafter referred to as cpx-absent amphibolites. At the microscopic scale, amphibolites exhibit a typical

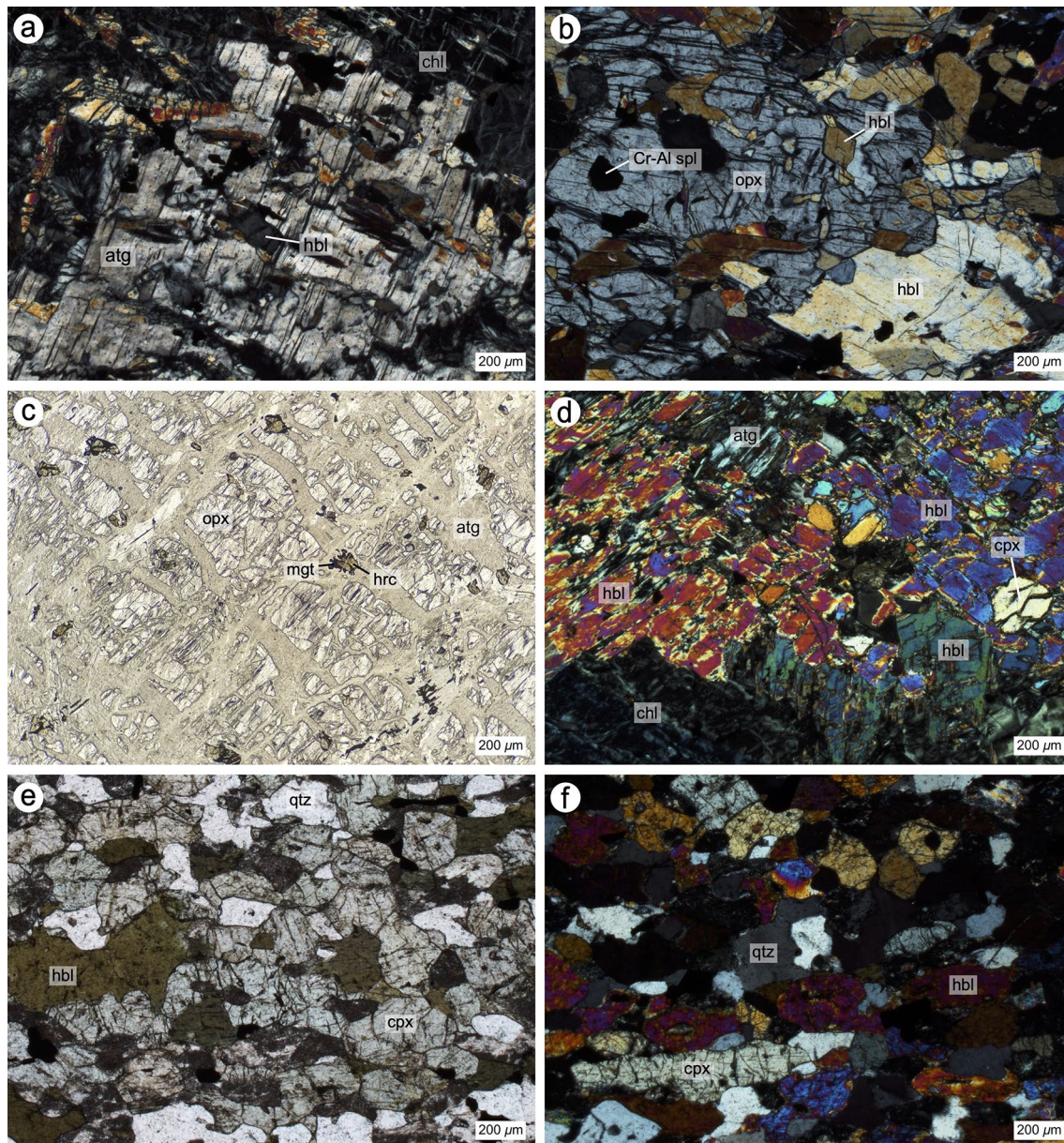


Fig. 3 Photomicrographs in cross-polarized light (**a**, **b**, **d**, and **f**) and plane-polarized light (**c** and **e**) illustrating mineralogy and textural features of USB rocks. **a** Ultramafic sample exhibiting an opx pseudomorph metamorphosed into antigorite containing an inclusion of hbl. **b** Subhedral to euhedral Cr–Al spl inclusion within millimeter-sized opx displaying a sharp contact with hbl in an ultramafic rock. Euhedral, millimeter-sized hbl also occur as inclusion within opx. **c** Centimeter-sized opx crystal altered to serpentine along cleavage planes within an ultramafic rock. The brownish to greenish hercynitic spl are located in the antigorite groundmass and systematically have

a magnetite rim. **d** Submillimetric cpx inclusions in hbl being surrounded by antigorite and chlorite (>90% of ultramafic rocks modal abundance) within the cpx-bearing ultramafic sample (IN16098b). **e** Amphibolite exhibiting a granoblastic texture associated with plag + amph + cpx + quartz + oxides paragenesis. **f** Fractured millimetric cpx in contact with amph + quartz within an amphibolite. The foliation is marked by elongated cpx and hbl. The subgrain boundaries of quartz are typical of metamorphic recrystallization. *atg* antigorite; *chl* chlorite; *hrc* hercynitic spl; *mgt* magnetite; *qtz* quartz. Other abbreviations as in the text

isogranular texture with a foliation marked by millimeter-sized cpx and amph (Fig. 3e, f), which may be green (Mg-hbl, tremolite, cummingtonite) to bluish green (pargasite). Except for their colors, Mg-hbl and pargasite share the same textural features. Tremolite often surrounds and grows on

top of Mg-hbl, pargasite, and cpx. These overgrowths and the presence of cummingtonite may be attributed to the metamorphic history of the massif. Most of the Mg-hbl and pargasite are in equilibrium with (1) millimeter-sized, partially sericitized plag, (2) quartz with undulose extinction

and subgrain boundaries that are features characteristic of plastic deformation, and (3) cpx having higher relief than amph (Fig. 3e, f). Subhedral titanite and ilmenite are present at grain boundaries (<0.1 mm). The texture and the mineral relationships suggest that amph cores and cpx cores surrounded by tremolite may be relics of a relatively high-grade metamorphic event alongside plag and cummingtonite, whereas tremolite probably formed as a result of retrograde metamorphic re-equilibration.

Rocks of sedimentary protolith

Banded-iron formations are mainly composed of alternating bands of Fe-oxides and silicates, which renders them a characteristic reddish color at weathering. Silicate layers record an NNW-striking mineral foliation parallel to the USB main structural grain. At the microscale, the Fe-oxides are associated with Fe-olivine, Fe-pyroxene, and Fe-amphibole, interpreted to form through the isochemical transformation of Fe-oxides and quartz during amphibolite facies metamorphism (e.g., Klein 2005).

Micaschists of probable detrital origin share the common NNW-striking foliation. They exhibit a grano-porphroblast texture with numerous aluminous phases such as garnet and biotite that can be used as a geothermometer. Porphyroblastic garnet (~2 mm) containing biotite and quartz inclusions is surrounded by often chloritized, prismatic, millimeter-sized biotite. Millimeter-sized plag and quartz with undulose extinction, as well as small amounts of ilmenite and magnetite, also occur.

Bulk-rock chemistry

Major and trace element concentrations allow us to distinguish between five different protoliths of magmatic origin in the USB (Table 1). The ultramafic rocks can be divided into two different groups according to their mineral assemblage and bulk-rock chemistry, whereas the amphibolites can be separated into three groups based on their bulk-rock chemistry and isotopic signature.

Ultramafic rocks

Ultramafic rocks can be subdivided into two groups according to their $\text{Al}_2\text{O}_3/\text{TiO}_2$ ratio and trace element concentrations (Figs. 4 and 5). The low $\text{Al}_2\text{O}_3/\text{TiO}_2$ (7–18) ultramafic rocks systematically lack opx while the high $\text{Al}_2\text{O}_3/\text{TiO}_2$ (20–70) group includes the cpx-absent, opx-bearing ultramafic sample (Fig. 4d). In the following, we use the mineralogical classification (i.e., cpx-bearing and cpx-absent) for clarity, although cpx and opx can be absent from the paragenesis. The cpx-bearing ultramafic rocks have high

Mg# [$100 \times \text{Mg}/(\text{Mg} + \text{Fe}_{\text{tot}})$; 86.3–91.7 mol.%] and low SiO_2 (37–49 wt.%) contents except for three samples with lower Mg# (65.7–76.2 mol.%; Fig. 4c). Their relatively high NiO contents (0.06–0.20 wt.%) is consistent with the initial presence of olivine. Chondrite-normalized rare earth element (REE) patterns exhibit enriched light REE (LREE; $1.22 < \text{La}_N/\text{Sm}_N < 12.38$) segments, slightly fractionated middle REE (MREE; $1.13 < \text{Sm}_N/\text{Dy}_N < 1.80$) segments, and rather flat heavy REE (HREE; $0.8 < \text{Dy}_N/\text{Yb}_N < 1.23$) segments except for two samples that are LREE-depleted ($0.60 < \text{La}_N/\text{Sm}_N < 0.85$) and one sample with a HREE-depleted ($\text{Dy}_N/\text{Yb}_N = 0.60$) segment (Fig. 5a). These samples have a variable Eu anomaly [$\text{Eu}^* = \text{Eu}_N/(\text{Sm}_N \times \text{Gd}_N)^{1/2}$] ranging from 0.60 to 3.16. Normalized to primitive mantle, cpx-bearing ultramafic rocks display a wide range of negative Nb anomalies [$\text{Nb}^* = \text{Nb}_N/(\text{K}_N \times \text{La}_N)^{1/2}$; 0.18–0.86; Fig. 5b).

The cpx-absent ultramafic rocks have Mg# (72.6–91.7 mol.%) and SiO_2 (39–47 wt.%) concentrations in the same range as the cpx-bearing samples (Fig. 4c). Bulk NiO content ranges from 0 to 0.15 wt.% suggesting the presence of moderate amounts of olivine in the protolith. Chondrite-normalized REE patterns show relatively enriched LREE ($0.86 < \text{La}_N/\text{Sm}_N < 2.46$) and HREE ($0.59 < \text{Dy}_N/\text{Yb}_N < 0.82$) segments resulting in U-shaped REE patterns (Fig. 5a). Most samples present a negative Eu anomaly (0.13–3.12). Normalized to primitive mantle, cpx-absent ultramafic rocks display slight U and Th combined with a pronounced negative Nb anomaly (0.06–0.31; Fig. 5b). A few samples may exhibit negative Zr and Hf anomalies [$\text{Zr}^* = \text{Zr}_N/(\text{Sm}_N \times \text{Nd}_N)^{1/2}$], but most have no Zr anomaly.

Amphibolites

Major and trace elements allow the distinction of three main groups of amphibolites in the USB. The first group, one of the two bearing cpx, has an average SiO_2 content of about 49 wt.% (46.5–53.3 wt.%) negatively correlated with Mg# (38.2–58.3 mol.%; Fig. 4c). These rocks have high TiO_2 contents (0.77–1.49 wt.%) resulting in low $\text{Al}_2\text{O}_3/\text{TiO}_2$ ratios (9–16; Fig. 4d) and high FeO (10.55–16.34 wt.%) contents typical of a tholeiitic signature (Fig. 4b). Chondrite-normalized REE patterns show flat HREE ($0.97 < \text{Dy}_N/\text{Yb}_N < 1.23$) and MREE ($0.97 < \text{Sm}_N/\text{Dy}_N < 1.47$) segments and slightly fractionated LREE ($0.74 < \text{La}_N/\text{Sm}_N < 1.62$) segments that highly resemble those of Archean tholeiites (Fig. 5c). Moreover, a slight positive Eu anomaly may occur in a few samples. These rocks display a negative Nb anomaly ($\text{Nb}^* = 0.15$ –0.86) and no Zr anomaly (Fig. 5d). Furthermore, these amphibolites present slightly negative to no $\mu^{142}\text{Nd}$ anomaly ($-3.4 < \mu^{142}\text{Nd} < 0.6$; Caro et al. 2017). Overall, these amphibolites have major and trace element concentrations characteristics of tholeiitic basalts (Figs. 4b

Table 1 Representative bulk-rock major and trace-element analyses of Ukaliq samples

	Ultramafic rocks			Amphibolites				
	Tholeiitic		Boninitic	Tholeiitic	Transitional	Boninitic	Calc-alkaline	
Major elements (wt.%)								
SiO ₂	41.46	46.82	42.51	44.20	48.88	50.08	50.26	52.24
TiO ₂	0.06	0.61	0.11	0.46	1.12	0.90	0.59	0.61
Al ₂ O ₃	0.63	6.96	5.93	11.43	14.41	14.29	14.12	16.58
MgO	34.57	15.91	30.38	20.85	7.15	8.07	9.61	5.82
Fe ₂ O ₃	8.25	12.92	8.36	14.30	14.01	12.13	11.85	10.42
MnO	0.13	0.22	0.13	0.18	0.24	0.22	0.24	0.20
CaO	3.96	11.83	2.53	3.42	9.50	8.61	8.09	8.40
Na ₂ O	0.04	0.70	0.25	0.87	1.86	2.37	1.65	2.97
K ₂ O	0.03	0.35	0.41	0.43	1.34	1.06	1.63	1.14
P ₂ O ₅	0.05	b.d	b.d	b.d	0.08	0.06	0.05	b.d
LOI	11.45	2.49	8.37	3.62	1.10	1.78	1.76	1.44
Total	99.24	98.80	99.00	99.76	99.67	99.54	99.81	99.82
Trace elements (µg g ⁻¹)								
Sc	5	25	24	38	43	40	44	49
V	20	141	87	184	285	252	229	221
Cr	930	2095	4251	1121	208	449	795	219
Ni	2195	765	1280	547	199	240	185	88
Cu	101	106	28	15	75	59	32	40
Zn	45	162	109	74	96	98	107	91
Cs	0.38	0.28	3.53	2.03	1.00	0.57	0.67	1.17
Rb	1.8	5.0	26.8	20.2	57.7	42.6	86.2	45.8
Sr	9.69	24.12	8.20	13.29	151	116	104	96
Y	2.197	12.41	3.927	10.42	24.4	20.6	14.6	18.4
Zr	4.78	49	5.78	33	65	66	37	63
Nb	0.254	2.82	0.210	1.50	2.68	2.51	1.42	2.93
Ba	4.41	36.3	8.08	67.7	181	82.8	122	104
La	1.58	5.20	0.371	1.68	4.41	5.04	3.21	8.83
Ce	2.8	11.1	0.84	3.5	10.9	11.4	7.1	18.4
Pr	0.316	1.53	0.111	0.505	1.66	1.63	0.984	2.25
Nd	1.26	6.83	0.491	2.41	8.28	7.81	4.58	9.22
Sm	0.313	1.80	0.166	0.845	2.66	2.43	1.41	2.21
Eu	0.102	0.625	0.047	0.255	0.998	0.855	0.513	0.733
Gd	0.345	1.95	0.274	1.15	3.26	2.91	1.75	2.42
Tb	0.056	0.333	0.061	0.231	0.598	0.524	0.329	0.440
Dy	0.361	2.16	0.522	1.69	4.10	3.53	2.32	2.87
Ho	0.078	0.472	0.138	0.408	0.926	0.785	0.536	0.614
Er	0.209	1.29	0.433	1.14	2.58	2.17	1.51	1.80
Tm	0.031	0.190	0.072	0.182	0.394	0.331	0.236	0.288
Yb	0.205	1.22	0.525	1.21	2.65	2.18	1.61	2.00
Lu	0.033	0.182	0.087	0.194	0.412	0.338	0.253	0.319
Hf	0.132	1.26	0.199	0.965	1.90	1.91	1.10	1.71
Ta	0.020	0.232	0.021	0.132	0.238	0.229	0.123	0.256
Pb	2.43	4.77	1.71	2.72	6.37	5.80	7.32	8.00
Th	0.109	0.788	0.126	0.674	0.431	1.23	0.536	2.12
U	0.097	0.347	0.079	0.174	0.149	0.313	0.158	0.511

The complete dataset is available in Electronic Supplementary Material (Table S1)

b.d. below detection

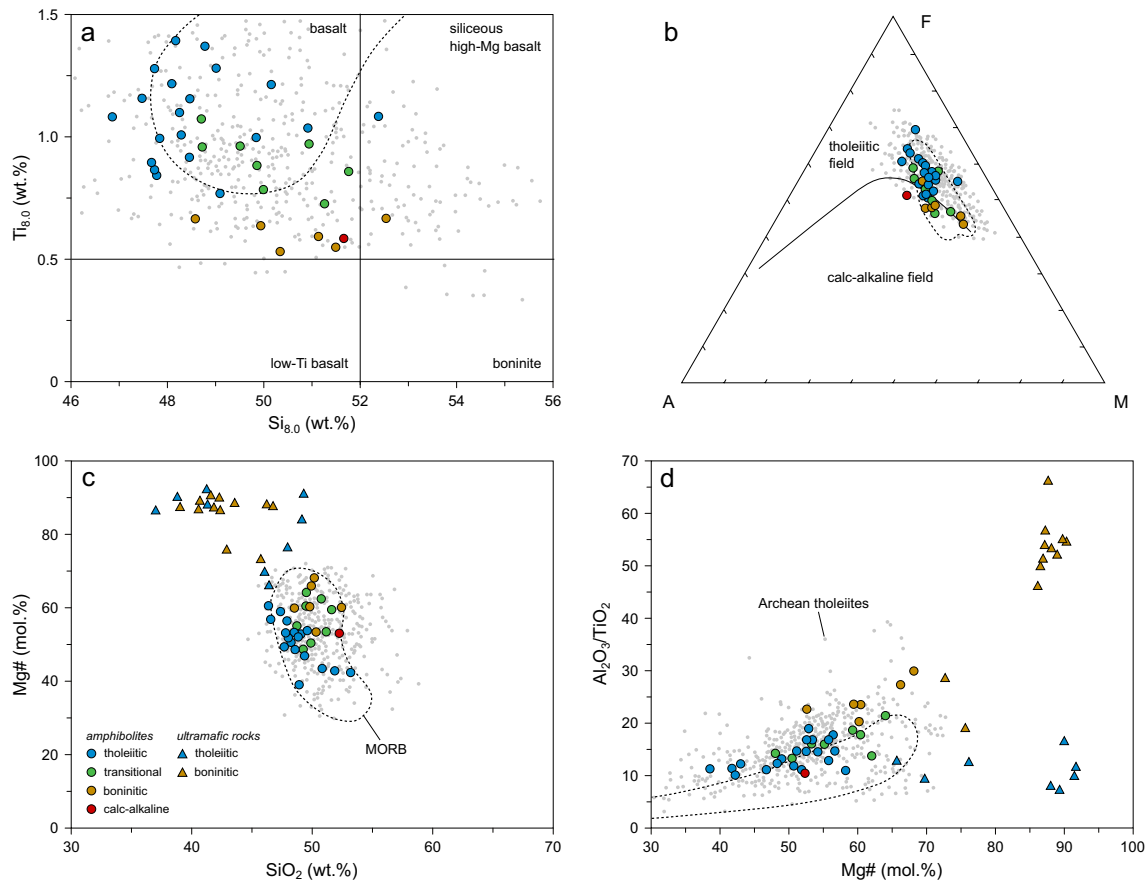


Fig. 4 Major element bulk-rock data of USB rocks. **a** $\text{Si}_{8.0}$ (wt.%) vs. $\text{Ti}_{8.0}$ (wt.%) boninite classification diagram from Pearce and Reagan (2019). **b** AFM (Alkalis–FeO–MgO) diagram discriminating tholeiitic compositions from calc-alkaline compositions (Irvine and Bar-

gar 1971). **c** SiO_2 (wt.%) vs. Mg# (mol.%). **d** Mg# (mol.%) vs. $\text{Al}_2\text{O}_3/\text{TiO}_2$. MORB (Gale et al. 2013) and Archean tholeiites (Georoc 2021) compositions are shown for comparison

and 5c) and will, therefore, be referred to as tholeiitic amphibolites. The cpx-bearing ultramafic samples have similar bulk-rock features and, together with the tholeiitic amphibolites, define a differentiation trend (Fig. 4d). Hence, these will be referred to as tholeiitic ultramafic rocks.

The second group of amphibolites, characterized by the absence of cpx, can be distinguished chemically from the tholeiitic amphibolites by their higher Mg# (52.5–68.1 mol.%), MgO (8.0–12.7 wt.%) and SiO_2 (48.5–52.5 wt.%) contents, and lower TiO_2 (0.49–0.67 wt.%) contents resulting in high $\text{Al}_2\text{O}_3/\text{TiO}_2$ ratios ranging from 23 to 30 (Fig. 4). A peculiarity of these samples lies in their low concentrations in incompatible elements ($\sum\text{REE} = 15.9\text{--}22.5$ ppm) compared to tholeiitic amphibolites ($\sum\text{REE} = 25.1\text{--}68.7$ ppm). Chondrite-normalized REE diagram exhibits a slight U-shaped pattern with LREE ($1.14 < \text{La}_N/\text{Sm}_N < 1.81$) and HREE ($0.85 < \text{Dy}_N/\text{Yb}_N < 0.98$) enrichments relative to MREE (Fig. 5g). These rocks display a strongly negative Nb–Ta anomaly ($\text{Nb}^* = 0.11\text{--}0.17$) and no Zr anomaly ($\text{Zr}^* = 0.85\text{--}1.17$) except for one sample

($\text{Zr}^* = 2.81$; Fig. 5h). Overall, amphibolites from this group resemble boninites from modern subduction settings (e.g., Reagan et al. 2010). Boninites are defined as volcanic rocks with high SiO_2 ($\text{Si}_{8.0} > 52$ wt.%) and MgO (> 8 wt.%) contents, and low TiO_2 ($\text{Ti}_{8.0} < 0.50$ wt.%) contents (Fig. 4a). They usually display a U-shaped REE pattern interpreted to reflect the addition of LREE-rich fluids to a highly depleted mantle source (Pearce and Reagan 2019). Compared to modern boninites, our samples are less depleted in REE and their bulk SiO_2 and TiO_2 contents do not satisfy all the conditions to qualify these samples as boninites *sensu stricto* (Fig. 4a). However, these rocks exhibit geochemical signatures resembling modern boninites (high MgO contents, low TiO_2 contents, and U-shaped REE pattern; Reagan et al. 2010; Taylor et al. 1994) and will thus be referred to as boninitic amphibolites. These boninite-like geochemical signatures are also found in the NSB and ISB (O’Neil et al. 2011; Szilas et al. 2015) and in recent ophiolitic complexes (e.g., Pearce and Robinson 2010). In addition, the cpx-absent ultramafic rocks display similar characteristics as the boninitic amphibolites

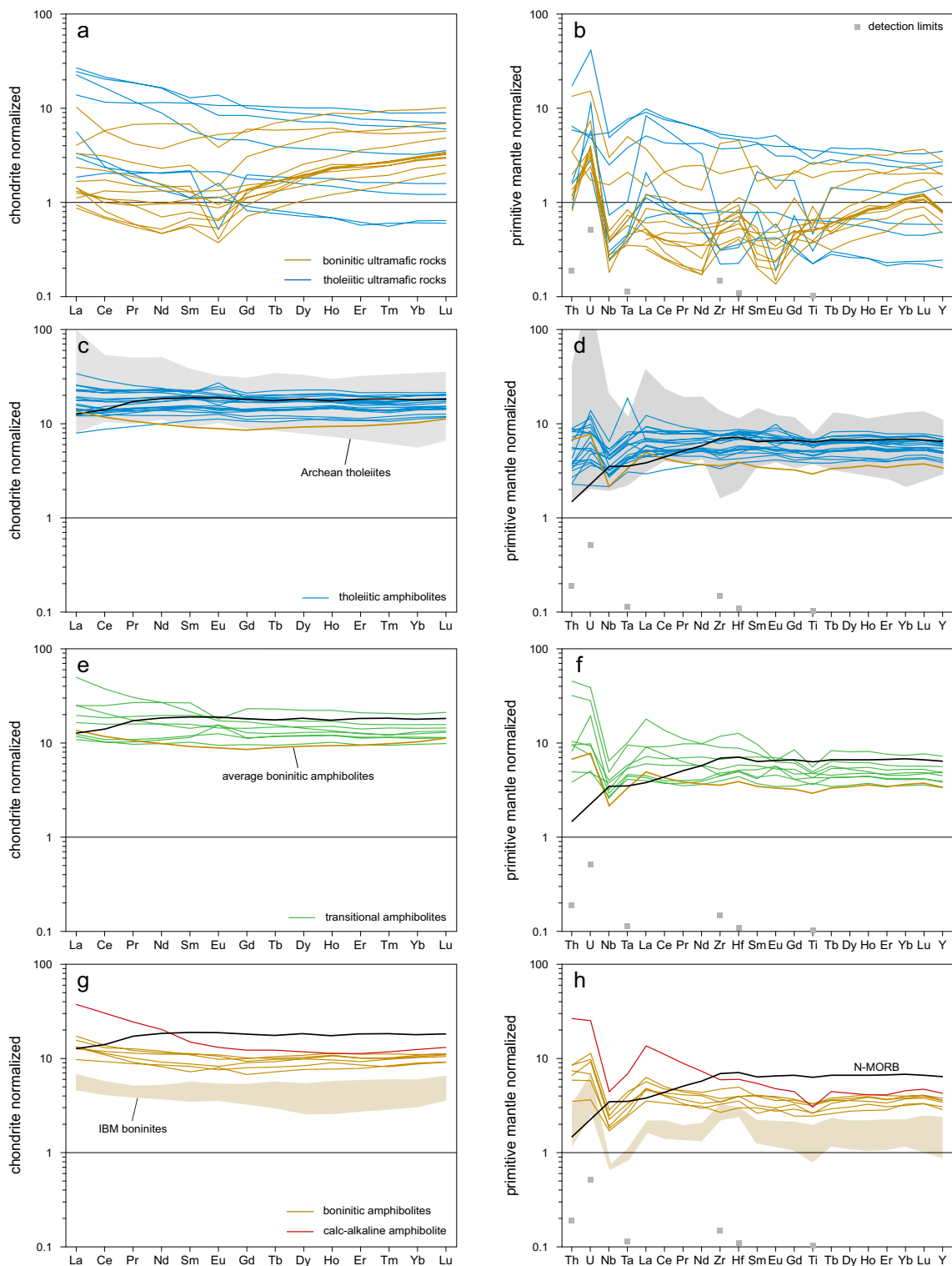


Fig. 5 Bulk-rock chondrite-normalized REE contents and primitive mantle-normalized trace element contents. **a, b** Tholeiitic and boninitic ultramafic rocks. **c, d** Tholeiitic amphibolites compared to N-MORB and the average boninitic amphibolite composition. **e, f** Transitional amphibolites compared to N-MORB and the average boninitic amphibolite composition. **g, h** Boninitic and calc-alkaline

amphibolites. N-MORB (Sun and McDonough 1989), Archean tholeiites (Georoc 2021), and Izu–Bonin boninites (Reagan et al. 2010) compositions are shown for comparison. Detection limits are also shown when possible. Normalized values are from Sun and McDonough (1989)

(low $\text{Al}_2\text{O}_3/\text{TiO}_2$ ratio, U-shaped REE pattern). As a result, they will be referred to as boninitic ultramafic rocks. The boninitic amphibolites can be further distinguished from the tholeiitic amphibolites by the presence of negative $\mu^{142}\text{Nd}$ anomalies ($-5.4 < \mu^{142}\text{Nd} < -3.7$; Caro et al. 2017).

The third group corresponds to transitional amphibolites with intermediate composition between tholeiitic amphibolites and boninitic amphibolites. Their SiO_2 contents (48.8–51.7 wt.%) and Mg# (48.1–64.1 mol.%) are similar to other amphibolite types, whereas their $\text{Al}_2\text{O}_3/\text{TiO}_2$ ratio (12.9–20.9) forms a continuum between the two categories mentioned above (Fig. 4). Their REE diagrams (Fig. 5e) exhibit flat HREE ($0.98 < \text{Dy}_\text{N}/\text{Yb}_\text{N} < 1.15$) segments coupled with a flat to negative LREE slope ($0.93 < \text{La}_\text{N}/\text{Sm}_\text{N} < 2.31$). Furthermore, REE concentrations are also intermediate between the tholeiitic and boninitic endmembers ($\sum\text{REE} = 25\text{--}41$ ppm). Primitive mantle normalized, transitional amphibolites display no Zr anomaly ($\text{Zr}^* = 0.83\text{--}1.20$) and a negative Nb anomaly ($\text{Nb}^* = 0.17\text{--}0.32$; Fig. 5f). In addition, their $\mu^{142}\text{Nd}$ signature is negative and similar to boninitic amphibolites ($-5.2 < \mu^{142}\text{Nd} < -3.2$; Caro et al. 2017). These amphibolites will thus be referred to as transitional amphibolites.

Apart from these three groups, one sample (IN12032) has an atypical chemistry that differs markedly from the other amphibolites. Although its SiO_2 content (52.2 wt.%) and Mg# (52.5 mol.%) are similar compared to previously described rocks (Fig. 4c), the TiO_2 content (0.61 wt.%) is as low as in boninitic amphibolites. However, this sample is different from the boninitic amphibolites by having higher REE concentrations ($\sum\text{REE} = 52.1$ ppm) typified by a strong LREE enrichment ($\text{La}_\text{N}/\text{Sm}_\text{N} = 4.0$) and a HREE depletion compared to N-MORB. When normalized to primitive mantle, this sample is shown to be enriched in large ion lithophile elements (LILE; $\text{Th}_\text{N} + \text{U}_\text{N} > 30$) and exhibits depletion in high field strength elements (HFSE) with a negative Nb–Ta anomaly ($\text{Nb}^* = 0.19$; Fig. 5h). The major and trace element concentrations of this sample are characteristic of calc-alkaline basalts (Fig. 4b) and will, therefore, be referred to as calc-alkaline amphibolite. In addition, this calc-alkaline sample carries the most negative $\mu^{142}\text{Nd}$ signature ($\mu^{142}\text{Nd} = -9.4$; Caro et al. 2017).

Mineral chemistry

The representative major and trace element analyses of cpx, opx, and amph from the ultramafic and mafic rocks are presented in Table 2. The complete dataset can be found in Electronic Supplementary Material 1 (Table S2).

Ultramafic rocks

The clinopyroxenes from the tholeiitic ultramafic rocks in our study do not present chemical zoning and belong to the diopside–hedenbergite solid-solution. They show homogeneous Mg# (93.7–94.7 mol.%) and variable Al^{IV} (0.01–0.06 a.p.f.u.) contents (Fig. 6a) positively correlated with TiO_2 (0.11–0.58 wt.%). The high TiO_2 and Al^{IV} grains have the highest Cr_2O_3 (~0.15 wt.%) contents, whereas the low TiO_2 and Al^{IV} grains have no chromium. Chondrite-normalized REE patterns show slightly fractionated HREE ($1.28 < \text{Dy}_\text{N}/\text{Yb}_\text{N} < 1.64$) and MREE ($0.97 < \text{Sm}_\text{N}/\text{Dy}_\text{N} < 1.47$) segments, and moderately fractionated LREE ($0.59 < \text{La}_\text{N}/\text{Sm}_\text{N} < 0.89$) segments (Fig. 6b) with little to no Eu anomaly. When primitive mantle normalized, cpx present Zr–Hf anomalies ranging from slightly negative ($\text{Zr}^* \approx 0.7$) to largely positive ($\text{Zr}^* > 1.8$).

Amphiboles from the tholeiitic ultramafic rock are dominantly Mg-hbl and tremolite, the latter forming rims around Mg-hbl. The transition from hbl core to tremolite rim is sharp, with Si increasing from 7.15 to 7.95 a.p.f.u., while $(\text{Na} + \text{K})^{\text{A}}$ and Al^{IV} decrease from 0.25 to 0 a.p.f.u. and from 0.75 to 0 a.p.f.u., respectively (Fig. 7). Mg-hbl delineate two distinctive trends of increasing TiO_2 (0–0.89 wt.%) contents with decreasing Mg# (Fig. 7c), probably representing two generations of amph. In both Mg# groups, high TiO_2 (> 0.1 wt.%) amphiboles also have high Cr_2O_3 (> 0.2 wt.%) contents, contrasting with the low Cr_2O_3 contents of tremolite. When chondrite normalized, Mg-hbl exhibit a smooth, nearly parallel pattern compared to cpx except for HREE being less fractionated ($\text{Dy}_\text{N}/\text{Yb}_\text{N} \approx 1.20$) and a small positive Eu anomaly (Fig. 7d). When primitive mantle normalized, Mg-hbl display slight U–Th enrichment and little to no HFSE depletion. Amphiboles from the boninitic ultramafic rocks are Mg-hbl and display increasing TiO_2 concentration with decreasing Mg# (Fig. 7c), which is negatively correlated with Cr_2O_3 , trending from 1.0 to 0.2 wt.% with decreasing Mg#. Chondrite normalized, these hbl have the same U-shaped REE pattern as their host rock typified by their low $(\text{Dy}/\text{Yb})_\text{N}$ values in the range of 0.68–0.69 and a small negative Eu anomaly (Fig. 7d). Normalized to primitive mantle, they display strong Nb, Ta, and Sr negative anomalies and U and Pb enrichments.

Millimeter- to centimeter-sized opx display a trend of increasing Al^{IV} (0.03–0.08 a.p.f.u.) contents with decreasing Mg# (88.6–85.8 mol.%). These major element values are in the range of opx derived from fractionation experiments at 0.5 GPa (Krawczynski et al. 2012) and opx from ultramafic arc and forearc cumulates (Fig. 8a). A second group of opx exhibits lower Mg# (74.9–76.7 mol.%) that are uncorrelated with Al^{IV} . Chondrite-normalized REE patterns for

Table 2 Representative major and trace element analyses of minerals from Ukaliq samples

	Ultramafic rocks				Amphibolite			
	Tholeiitic		Boninitic		Tholeiitic		Transitional	
	Cpx	Amph	Opx	Amph	Cpx	Amph	Cpx	Amph
Major elements (wt.%)								
SiO ₂	54.32	50.64	56.45	49.63	51.04	46.62	52.62	44.56
TiO ₂	0.31	0.56	0.05	0.35	0.11	0.77	0.08	1.06
Al ₂ O ₃	1.23	7.30	1.85	9.58	0.84	7.71	0.73	9.87
Cr ₂ O ₃	0.08	0.43	0.09	0.46	0.01	0.05	0.07	0.36
FeO	1.84	6.03	9.02	4.49	16.33	22.25	12.28	18.74
MnO	0.07	0.09	0.18	0.09	0.38	0.33	0.54	0.35
MgO	17.24	19.13	32.98	19.68	9.01	10.70	11.48	9.49
CaO	25.86	12.40	0.13	12.14	22.62	8.38	22.86	11.79
Na ₂ O	0.02	1.07	0.01	1.41	0.24	0.92	0.26	1.03
K ₂ O	0.00	0.17	0.00	0.25	0.00	0.34	0.00	1.08
Total	100.99	97.86	100.78	98.15	100.60	98.08	100.95	98.37
Trace elements (µg g ⁻¹)								
Li	2.7	0.9	3.1	1.5	11.5	4.8	12.6	1.9
B	3.0	6.3	2.8	2.4	1.3	1.4	1.2	1.6
Sc	20.5	59.0	19.5	44.2	64.2	77.3	31.1	67.7
V	62.5	218	64	191	249	717	108	379
Cr	666	3516	484	3446	102	493	481	3718
Mn	543	421	1383	645	2971	1928	5369	3254
Co	13.8	28.1	52.8	29.8	42.2	54.7	66.1	94.4
Ni	158	510	490	787	65	144	162	392
Cu	0.099	0.728	0.698	0.422	1.17	0.707	0.226	0.504
Zn	8.6	15.9	22.0	6.4	106	190	129	205
Rb	0.04	0.91	0.26	0.37	0.12	5.02	0.04	5.26
Sr	6.92	41.7	0.28	6.99	19.5	43.3	11.6	25.2
Y	3.03	18.49	0.11	7.56	12.99	65.40	4.07	31.14
Zr	16.6	63.4	0.401	9.4	8.6	20.3	5.5	36.0
Nb	0.175	4.87	0.172	0.305	0.024	5.97	0.004	2.74
Mo	0.021	0.036	0.098	0.032	0.084	0.104	0.184	0.208
Cs	0.108	0.034	0.147	0.024	0.022	0.156	0.022	b.d
Ba	0.078	0.66	0.15	0.49	0.38	44.9	0.17	38.8
La	0.640	6.62	0.009	1.24	0.883	7.48	0.421	3.39
Ce	1.86	15.3	0.044	2.92	3.86	26.3	1.31	9.70
Pr	0.277	1.96	0.010	0.325	0.744	4.37	0.202	1.45
Nd	1.49	9.92	0.006	1.39	4.31	23.7	1.08	7.93
Sm	0.506	2.98	0.001	0.424	1.57	7.89	0.380	2.77
Eu	0.211	1.47	0.010	0.136	0.359	2.10	0.107	0.733
Gd	0.573	3.35	0.010	0.651	1.92	10.04	0.479	3.88
Tb	0.095	0.519	0.006	0.133	0.343	1.71	0.088	0.672
Dy	0.610	3.47	0.013	1.13	2.45	11.98	0.675	5.12
Ho	0.117	0.698	0.005	0.275	0.511	2.53	0.154	1.13
Er	0.314	2.00	0.021	0.918	1.51	7.33	0.474	3.38
Tm	0.043	0.289	0.013	0.151	0.239	1.05	0.074	0.491
Yb	0.282	1.94	0.071	1.07	1.84	6.67	0.567	3.15
Lu	0.041	0.320	0.016	0.158	0.347	0.900	0.099	0.453
Hf	0.456	1.66	0.023	0.260	0.469	1.41	0.150	1.29
Ta	0.030	0.233	0.800	0.017	0.003	0.568	0.002	0.166
Pb	0.208	2.69	0.167	1.18	1.14	7.27	1.23	3.24
Th	0.043	0.613	0.008	0.109	0.010	0.110	0.025	0.312
U	0.039	0.318	0.078	0.176	0.009	0.086	0.008	0.074

The complete dataset is available in Electronic Supplementary Material (Table S2)

b.d. below detection

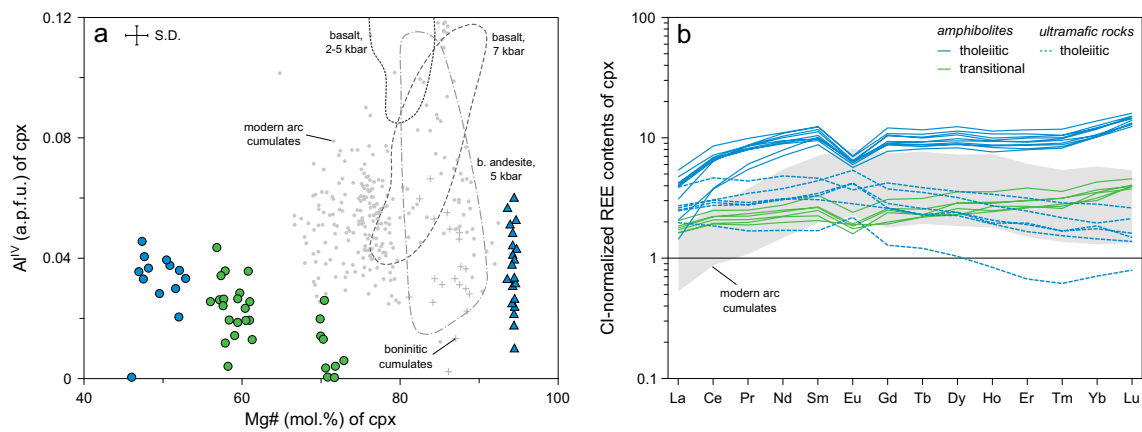


Fig. 6 Major and trace element compositions of cpx. **a** Mg# (mol.%) vs. Al^{IV} (a.p.f.u.). **b** Chondrite-normalized REE pattern of cpx from ultramafic rocks and amphibolites. Clinopyroxene compositions from modern arc cumulates (Bouilhol et al. 2015; Greene et al. 2006; Jagoutz et al. 2007; Otamendi et al. 2010; Walker et al. 2015), and boninitic cumulates (Bénard et al. 2018) are shown for comparison. Frac-

tionation experiments covering a wide range of pressures and starting material compositions (Feig et al. 2006; Krawczynski et al. 2012; Villiger et al. 2007) are also represented. Normalization values are from Sun and McDonough (1989). CI CI-type chondrite; S.D. standard deviation

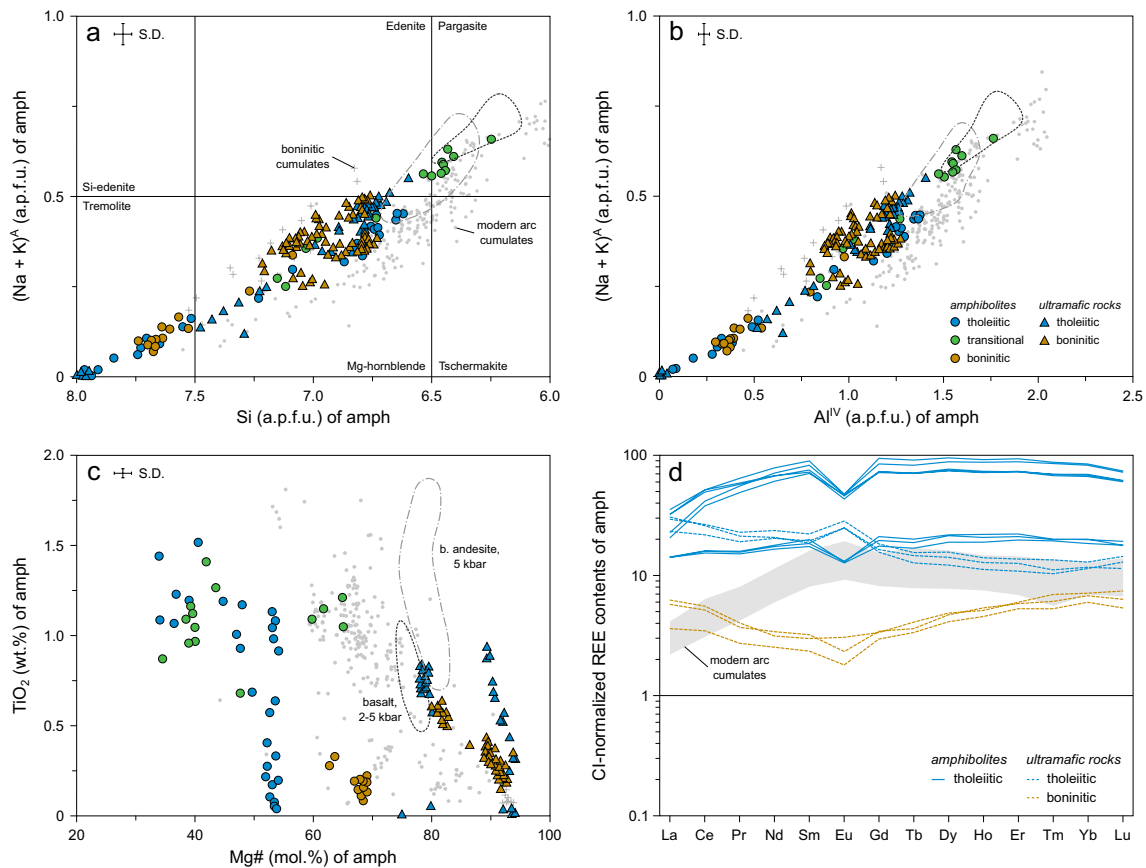


Fig. 7 Major and trace element compositions of amph. **a** Si (a.p.f.u.) vs. (Na + K)^A (a.p.f.u.) amph classification diagram of Leake (1978). **b** Al^{IV} (a.p.f.u.) vs. (Na + K)^A (a.p.f.u.) highlighting the temperature-dependent edenite exchange in amphibolites. **c** Mg# (mol.%) vs. TiO₂ (wt.%) of amph from ultramafic rocks and amphibolites. Amphibole compositions from modern arc cumulates (Bouilhol et al. 2015; Greene et al. 2006; Jagoutz et al.

2007; Otamendi et al. 2010; Walker et al. 2015), and boninitic cumulates (Bénard et al. 2018) are shown for comparison. Fractionation experiments covering a wide range of pressures and starting material compositions (Feig et al. 2006; Krawczynski et al. 2012) are also represented. Amphibole did not crystallize in the experiments of Villiger et al. (2007). Normalization values are from Sun and McDonough (1989). CI CI-type chondrite; S.D. standard deviation

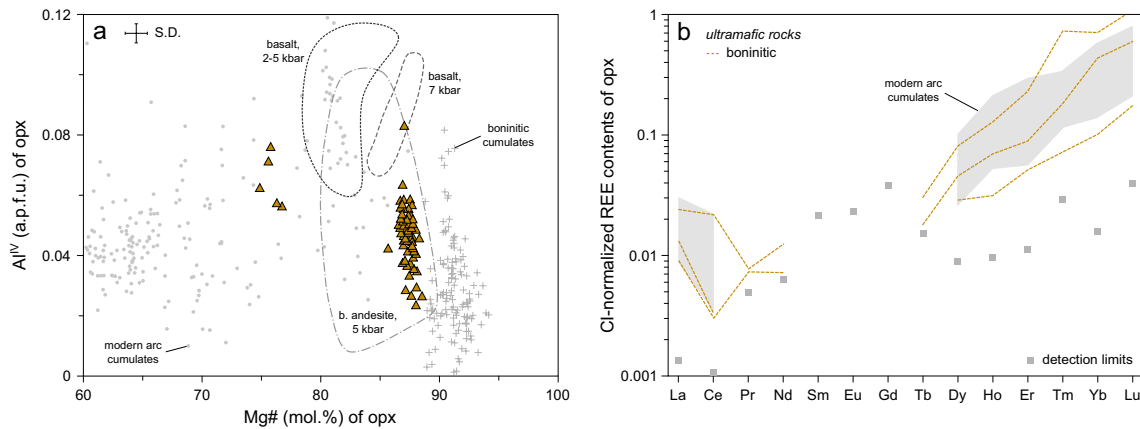


Fig. 8 Major and trace element compositions of opx. **a** Mg# (mol.%) vs. Al^{IV} (a.p.f.u.). **b** Chondrite-normalized REE pattern of opx from ultramafic rocks. Orthopyroxene compositions from modern arc cumulates (Bouilhol et al. 2015; Greene et al. 2006; Jagoutz et al. 2007; Otamendi et al. 2010; Walker et al. 2015), and boninitic cumulates (Bénaud et al. 2018) are shown for comparison, as well as frac-

tionation experiments covering a wide range of pressures and starting material compositions (Feig et al. 2006; Krawczynski et al. 2012; Viliger et al. 2007). Detection limits are also represented. Normalization values are from Sun and McDonough (1989). CI CI-type chondrite; S.D. standard deviation

opx display a highly fractionated MREE to HREE pattern, with (Sm/Yb)_N varying from 0.003 to 0.09 and a contrasting negative LREE slope (Fig. 8b).

Dark spl (Electronic Supplementary Material ESM 2) define a correlation of increasing Cr# [100 × Cr/(Cr + Al + Fe³⁺); 19.9–49.4 mol.%] with decreasing Mg# (65.1–40.7 mol.%). A chemical zoning is observed with a decrease of Cr₂O₃ content from core to rim. This trend of increasing Cr# with decreasing Mg# (Cr–Al trend of Barnes and Roeder 2001) is interpreted to reflect equilibrium with a ferromagnesian phase such as pyroxene or olivine (Irvine 1967). Hercynitic spl display low Cr# (5.2–8.8 mol.%) and high Mg# (48.3–70.8 mol.%), which cannot be used to decipher between magmatic and metamorphic compositions. Magnetites from boninitic ultramafic rocks are pure magnetite, whereas magnetites from tholeiitic samples are Cr-magnetite with Cr³⁺ > 0.6 a.p.f.u.

Antigorite from the cpx-bearing group has high Mg# (89.5–90.9 mol.%), low Al₂O₃ (0.84–1.20 wt.%) concentrations, and NiO content ranging from 0 to 0.11 wt.%. Then again, antigorite from the cpx-absent group has slightly lower Mg# (87.3–88.3 mol.%), and higher Al₂O₃ (2.44–3.36 wt.%) and NiO (0.14–0.15 wt.%) content values. We interpret the high-NiO antigorite as most likely olivine pseudomorphs, whereas the high-Al₂O₃ antigorite possibly reflects an opx-rich protolith.

Amphibolites

Clinopyroxenes from tholeiitic and transitional amphibolites have a wide range of Mg# (46.2–73.1 mol.%) and display rough trends of decreasing Mg# with increasing

Al^{IV} concentrations (Fig. 6a). Chondrite-normalized REE patterns show flat HREE (0.80 < Dy_N/Yb_N < 0.95) and MREE (0.89 < Sm_N/Dy_N < 1.12) segments, whereas LREE (0.14 < La_N/Sm_N < 0.70) are moderately fractionated (Fig. 6b). The cpx display a negative Eu anomaly ranging from 0.58 to 0.96.

Amphiboles from tholeiitic and transitional amphibolites range from Mg-hbl to pargasite and are often surrounded by retrogression tremolite (Fig. 7a). The Mg-hbl and pargasite display a broad range of Mg# from 36.1 to 69.2 mol.% uncorrelated to TiO₂ (Fig. 7c). Chondrite normalized, Mg-hbl exhibit a nearly parallel pattern compared to cpx from mafic rocks, but with higher concentrations. Pargasites were not analyzed for their trace elements. Amphiboles from boninitic amphibolites are cummingtonite, corresponding to CaO-poor (0.40–1.17 wt.%) amph. Overall, cpx and amph from amphibolites are chemically zoned with Al₂O₃-, TiO₂- and Cr₂O₃-rich cores that differ from tremolite rims which usually display depletion in the aforementioned elements.

Plagioclase from tholeiitic amphibolites have compositions ranging from labradorite to andesine with high Ca (0.23–0.71 a.p.f.u.) and Na (0.29–0.73 a.p.f.u.) contents (An_{24–71}), whereas K concentrations (0.00–0.01 a.p.f.u.) are low. The plag from boninitic amphibolites were not analyzed.

Pressure–temperature constraints

In this section, we use phase equilibria modeling and geothermometers to assess the equilibrium conditions of the USB rock phases. This allows distinguishing between

medium-to-high temperature metamorphism and higher temperatures, magmatism-related phase crystallization. The mineral assemblage of the micaschists allows the determination of pressure and temperature conditions of the last metamorphic peak experienced by the Innuksuac complex. The paragenesis of sample IN16164 is biotite + garnet + plag + quartz + chlorite + ilmenite + magnetite and contains 7–9 vol.% garnet with an almandine-rich composition (Alm_{71} , Prp_{15} , $Grss_{10}$, $Spss_4$). Pseudosections were calculated by Gibbs energy minimization using *Perple_X* (version 6.9.1; Connolly 2005) and the self-consistent thermodynamic database of Holland and Powell (2011) in the system NCKFMASHTO. The selected solution models and the chosen H_2O and O_2 contents are discussed in the Electronic Supplementary Material ESM 2. The pressure–temperature equilibrium phase diagram calculated for sample IN16164 reveals that the observed assemblage is stable from 3 to 7 kbar and 580–630 °C (Fig. 9). Garnet isopleths and isochores further narrow the domain of equilibrium of our sample to 4–5.5 kbar and 615 ± 10 °C. To strengthen the thermodynamically inferred temperatures, paired analyses on garnet and biotite have been performed on the same sample. Temperatures are calculated based on the garnet–biotite thermometer of Ferry and Spear (1978) and are consistent

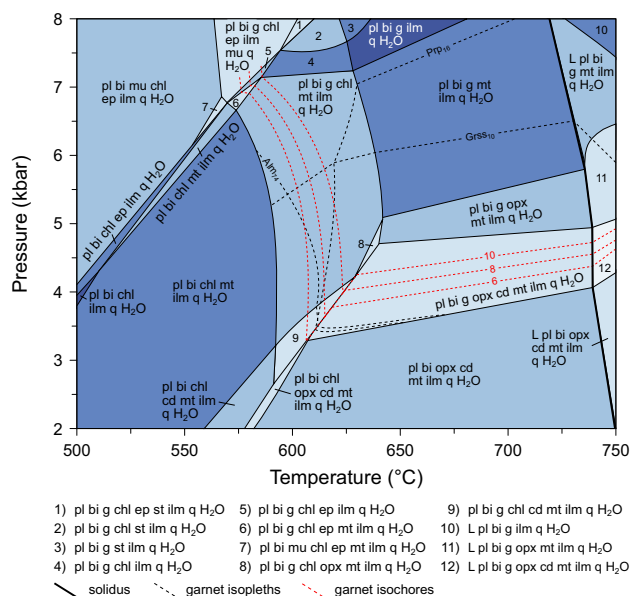


Fig. 9 NCKFMASHTO pressure–temperature pseudosection calculated using a micaschist composition (IN16164). The value for O_2 , representing the Fe_2O_3 component, was set to give a $Fe_2O_3/(FeO+Fe_2O_3)$ value of ~ 0.1 , and initial H_2O content was set in excess (Electronic Supplementary Material ESM 2). Garnet isopleths (Alm_{74} , Prp_{16} , $Grss_{10}$) and isochores (6, 8, and 10 vol.% garnet) are used to constrain the peak pressure–temperature conditions underwent by the USB. *bi* biotite; *cd* cordierite; *chl* chlorite; *ep* epidote; *g* garnet; *ilm* ilmenite; *L* silicate melt; *mt* magnetite; *mu* muscovite; *pl* plagioclase; *q* quartz. Other abbreviations as in the text

within error (593 ± 35 °C) with the modeled pseudosection. Similar garnet–biotite temperatures (580 ± 20 °C) are reported in the NSB (Cates and Mojzsis 2009).

Amphibole compositions have been shown to be temperature and/or pressure dependent (e.g., Holland and Blundy 1994). However, Al^{VI} and Ti contents from USB amph display no correlation with Al^{IV} , indicating that the pressure-dependent Al–Tschermak and temperature-dependent Ti–Tschermak exchanges only played a minor role. As shown in Fig. 7b, the dominant vector controlling amph chemistry is the temperature-dependent edenite exchange, suggesting that the evolution in $(Na+K)^A$ is controlled by cooling at constant pressure. As such, Ti-dependent amph thermometers (e.g., Putirka 2016) cannot be used to constrain the crystallization temperature of amph from the USB ultramafic rocks. We thus applied the edenite exchange-based amph–plag thermometer of Holland and Blundy (1994) which gives temperatures of 704 ± 47 °C for the amphibolites, slightly higher than the amph–plag temperatures (≤ 680 °C) reported for the NSB (Cates and Mojzsis 2009).

To determine the equilibrium conditions of opx from the boninitic ultramafic rocks, we used the Ca-in-opx thermometer of Brey and Köhler (1990). Assuming that the opx from USB equilibrated at 0.5 GPa, we obtain temperatures ranging from 820 to 980 °C. Despite its pressure dependency, the Ca-in-opx thermometer is almost insensitive to pressure changes, with an increase of 10 °C for a pressure of 0.8 GPa. The two-pyroxene thermometers are not employed as cpx and opx are never found in equilibrium in USB rocks.

Discussion

In this section, we use phase relationships, bulk-rock and mineral chemistry, and thermometry to unravel the metamorphic signal from the original magmatic signal and reconstruct the cumulate sequence followed by tholeiitic and boninitic melts by characterizing the most primitive magmas and their associated liquid lines of descent.

Magmatic signal preservation

It is evident from the mineralogy and pseudosection modeling that the USB underwent at least one metamorphic episode that reached amphibolite facies conditions. In detail, the Innuksuac complex experienced at least two metamorphic episodes (3622 ± 46 Ma and 2738 ± 25 Ma) at the amphibolite facies (Cates and Mojzsis 2007, 2009). These episodes probably correspond to magmatic intrusions of the Voizel and Boizard suites, respectively (e.g., Greer et al. 2020). These metamorphic events also likely modified the most fluid-mobile element concentrations of the USB rock suites. To assess the degree of preservation

of the original magmatic signal, we used the correlation-based method of Cann (1970). This method relies on the degree of correlation of any given element with Zr, considered fluid-immobile (e.g., Fraser et al. 1997). A theoretical crystallization vector can be drawn for each plot and each lithological unit, allowing the identification of uncorrelated, altered samples (Pearce 2014b). It is important to note that ultramafic rocks cannot be considered in the crystallization vector because they do not have a liquid composition (see below). Nevertheless, an identification of the altered samples will be attempted. As shown in Fig. 10a, a good correlation is found between Zr and Th, except for 2 tholeiitic amphibolites characterized by slightly lower Th contents. Overall, the REE also present a good correlation with Zr except for 3 tholeiitic ultramafic rocks that are La-rich and Yb-poor (Fig. 10b, c). The Nb vs. Zr diagram also shows a good correlation for every unit (Fig. 10d). Similar conclusions can be drawn for SiO₂ and MgO. In contrast, fluid-mobile elements (not plotted) display poor correlations with Zr, which can be interpreted as a magmatic signal, reflecting variable fluid-mediated LILE enrichments in the source or as a late metasomatic overprint. These processes are not mutually

exclusive but cannot be distinguished based on trace and major element chemistry alone. As such, only REE, HFSE, Y, and Th concentrations will now be considered representative of the magmatic signal and used further. These conclusions are consistent with the expected immobility of Th, Y, REE, and HFSE, and mobility of LILE during fluid circulation (Pearce 2014a, b).

Interpretation of mineral textures and chemistry

Mineral textures and chemistry and thermometric constraints described in the previous sections allow us to infer the metamorphic peak and discuss the origin (metamorphic vs. magmatic) of the different minerals constituting the USB rocks.

For the ultramafic rocks, the equilibrium paragenesis consisting of antigorite + chlorite + magnetite + tremolite is typical of greenschist to lower amphibolite facies conditions (< 600 °C), witnessing the retrogression of the ultramafic rocks. At the pressure–temperature conditions calculated using thermodynamic modeling (Fig. 9) and garnet–biotite and amph–plag thermometers, secondary olivine and opx could be present (Spear 1993). As such, the origin of the

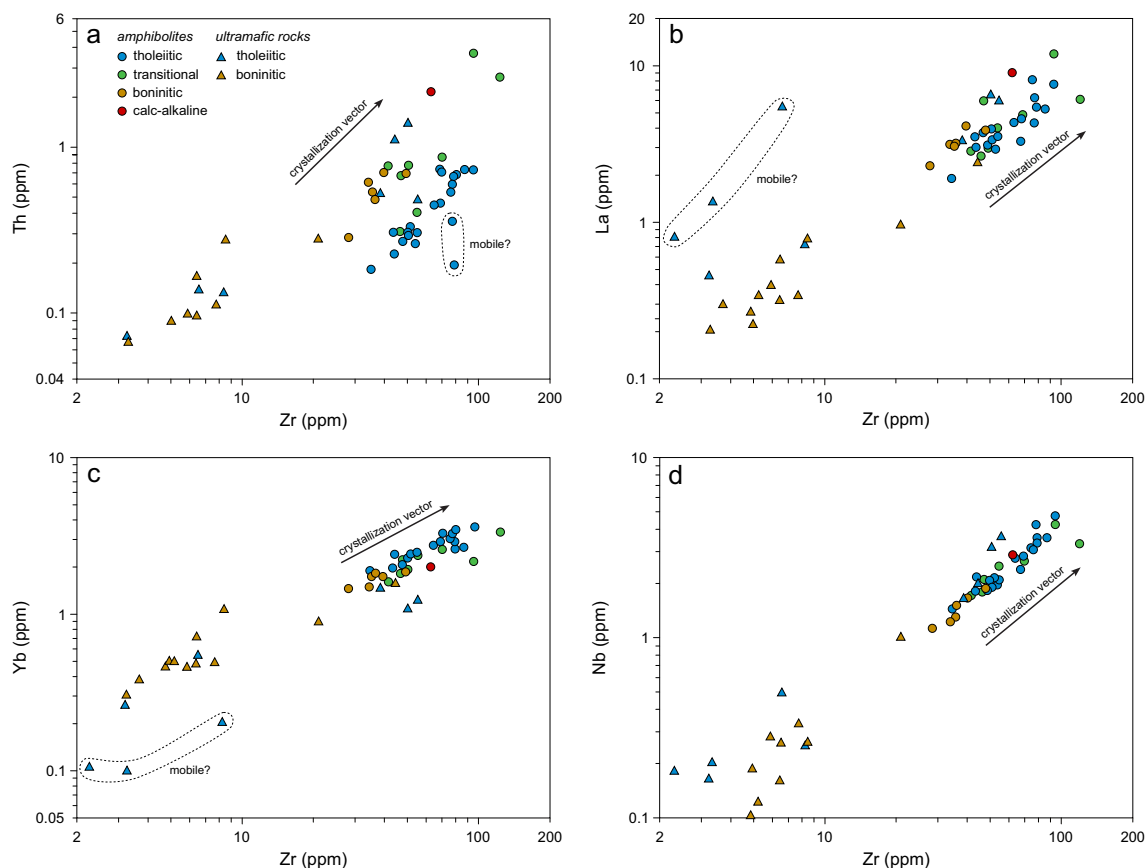


Fig. 10 Methodology for identifying mobile elements using bulk-rock compositions (based on Cann 1970 and Pearce 2014b). **a** Zr (ppm) vs. Th (ppm). **b** Zr (ppm) vs. La (ppm). **c** Zr (ppm) vs. Yb (ppm).

d Zr (ppm) vs. Nb (ppm). Theoretical vectors show the covariation expected during crystallization

observed opx must be addressed. The large size (> 5 mm) and optical continuity of opx, the inclusion of Cr-spl, and their calculated equilibrium temperatures (~980 °C) much above the metamorphic overprint point to a magmatic origin. In addition, the opx from the fractionation experiments of Krawczynski et al. (2012) at 0.5 GPa have similar compositions and crystallize in the same range of temperatures (950–1000 °C) as the opx from USB. As such, we interpret the opx to be of magmatic origin and their trace element concentrations representative of the liquid from which it crystallized. The trace element concentrations observed here are also similar to those found in modern arc to forearc environments (e.g., Jagoutz et al. 2007), strengthening the magmatic origin for the opx. Furthermore, the original magmatic signal is probably preserved for the slow-diffusing elements present in tetrahedrally coordinated sites (e.g., Cr, Al, Ti, and REE; Cherniak and Liang 2012; Ganguly et al. 2007). Indeed, the Cr diffusion closure temperature in opx has been defined at 870 °C for an initial temperature of 900 °C (Ganguly et al. 2007).

The origin of cpx and Mg-hbl in the ultramafic rocks is more challenging to assess because of the lack of inferred equilibrium temperatures. The cpx major element compositions show a wide range of Al₂O₃, Cr₂O₃, and TiO₂ contents for a near-constant Mg#. Low TiO₂ and Cr₂O₃ cpx are greenschist facies re-equilibrated cpx, but the high-TiO₂ grains point towards a magmatic origin. Indeed, if they were metamorphic, temperatures above 800 °C would be needed to stabilize cpx (Spears 1993), which is much higher than the peak temperature recorded here. The cpx major element compositions are relatively common in cumulative rocks, and elemental variations at a constant Mg# can reflect a reactional origin of the grains (melt–rock reaction) whereby the Mg# is buffered by the percolated rock, and, for example, the high TiO₂ contents reflect the reacting melt. If correct, then the trace element concentrations can be used to evaluate the liquid in equilibrium with the cpx. Interestingly, the observed cpx compositions are similar to those found in cumulative reactional pathways of magmatic arc systems that have drained damp tholeiitic melts (e.g., Chilas complex, Kohistan; Jagoutz et al. 2007).

Two types of amphibole can be observed in the ultramafic rocks, whereby Mg-hbl almost systematically show a retrogression to tremolite. These Mg-hbl are often found as inclusion or intimately related to the pyroxenes (Fig. 3) and have magmatic characteristics, such as high Cr₂O₃ and TiO₂ contents showing trends correlated with Mg#. Their major element compositions are often found in arc cumulates (Bouilhol et al. 2015; Cooper et al. 2016; Jagoutz et al. 2007) and experimental studies (Feig et al. 2006; Krawczynski et al. 2012; Nandedkar et al. 2014). Interestingly, Mg-hbl have near-parallel REE patterns and similar concentrations to the opx in the boninitic ultramafic rocks and the cpx in the

tholeiitic ultramafic rocks. Such feature is symptomatic of a co-magmatic origin for Mg-hbl and the pyroxenes (Adam and Green 2006; Bouilhol et al. 2015; Tribuzio et al. 2000). On the other hand, the slight positive Eu anomaly of Mg-hbl from the tholeiitic ultramafic samples could reflect a metamorphic origin whereby Mg-hbl replace plagioclase resulting in high Eu contents and a negative REE slope (Helmy et al. 2008). In all cases, the lack of calculated equilibrium temperatures for these Mg-hbl hampers our ability to constrain their origin unambiguously.

The amphibolites display a granoblastic texture associated with amphibole–plagioclase temperatures of ~700 °C, which is typical for mafic rocks that underwent amphibolite facies metamorphism. Further, both cpx and Mg-hbl show negative Eu and Sr anomalies, relatively flat HREE segments, and have nearly parallel REE patterns, with Mg-hbl being more enriched than cpx by an order of magnitude. Together with a well-equilibrated microtexture, these features call for a global chemical equilibrium between the amphibolite-bearing phases.

Overall, opx, cpx, and probably Mg-hbl from ultramafic rocks most likely represent the only primary igneous crystals in the USB rocks that can further be used to infer a crystallization sequence. Finally, the upper bound of the metamorphic peak experienced by the USB might be placed at 720 °C, which corresponds to the onset of partial melting of the metasediments, a feature not observed throughout the Innuksuac complex.

Protoliths of Ukaliq mafic and ultramafic rocks

Ukaliq ultramafic rocks display major element concentrations typical of dunite (SiO₂ = 40–42 wt.%), pyroxenite (SiO₂ = 48–52 wt.%) and (hbl-)gabbro (SiO₂ = 46–48 wt.%, Mg# ≈ 70 mol.%). More specifically, the tholeiitic ultramafic rocks have SiO₂/MgO (1.0–3.8) and Al₂O₃/CaO (0–0.7) ratios, as well as Al₂O₃ contents (0–6.8 wt.%) indicative of the former presence of olivine, cpx, plagioclase, and amphibole in the protolith (Fig. 11). In detail, one sample has high SiO₂/MgO and Al₂O₃ contents, and most likely crystallized plagioclase, and two samples located between the cpx and amphibole fields probably formed limited amounts of amphibole. On the other hand, the boninitic ultramafic rocks span a wide range of Al₂O₃/CaO values (1.0–11.1) and Al₂O₃ contents (4.1–15.9 wt.%) and have lower SiO₂/MgO values (1.2–2.4) rather pointing to large amounts of olivine, opx, and spl in their protoliths (Fig. 11). The former presence of olivine in both tholeiitic and boninitic ultramafic samples is further evidenced by the high bulk-rock and antigorite NiO contents. Such observations agree well with the observed opx–cpx dichotomy in the ultramafic rocks and characterize these ultramafic rocks as former dunite, wehrlite, orthopyroxenite, and (hbl-)gabbro. The presence of opx phenocrysts in ultramafic rocks

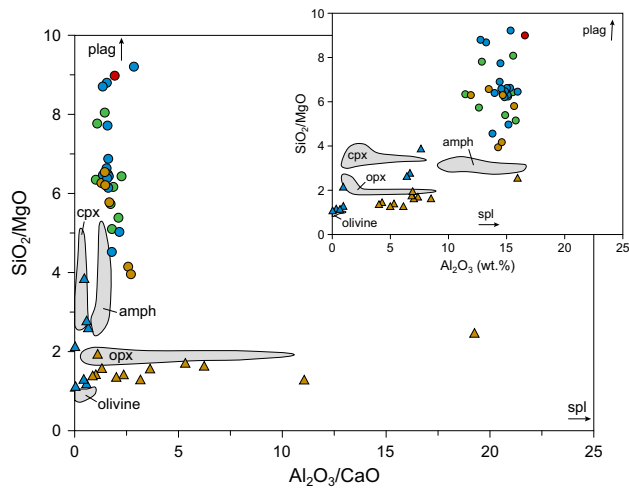


Fig. 11 Ukalik major element bulk-rock compositions used to identify the protolith initial mineralogy and plotted as $\text{Al}_2\text{O}_3/\text{CaO}$ vs. SiO_2/MgO . The top right panel shows the Al_2O_3 (wt.%) vs. SiO_2/MgO diagram used to constrain the presence of plag in the protoliths. The mineral compositions are compiled from modern arc cumulates (Bouilhol et al. 2015; Greene et al. 2006; Jagoutz et al. 2007; Otamendi et al. 2010; Walker et al. 2015) and crystallization experiments (Feig et al. 2006; Krawczynski et al. 2012; Villiger et al. 2007). Legend as in previous figures. Abbreviations as in the text

and the occurrence of dunite-, pyroxenite-, and gabbro-type rocks are usually related to cumulates during melt evolution. This cumulative origin is well demonstrated by the bulk-rock Mg# of the ultramafic rocks that range from 72 to 90 mol.%, whereas the mantle has higher Mg# (e.g., Bodinier and Godard 2014). The compatible element contents, such as Ni, Cr, and V, also indicate a cumulate origin for the ultramafic rocks. Indeed, refractory mantle rocks have Ni contents up to 3000 ppm, whereas pyroxenitic cumulates have concentrations ranging from 200 to 1400 ppm (e.g., Bodinier and Godard 2014; Bouilhol et al. 2009, 2015). As with the bulk-rock chemistry, the mineral compositions also point to a cumulative origin rather than a mantle origin. Clinopyroxenes from the tholeiitic ultramafic rock have REE concentrations up to ten times the chondrite values, while cpx from the sub-arc mantle and from abyssal peridotites have LREE content values ten to a hundred times lower than chondrite (Bodinier and Godard 2014; Bouilhol et al. 2009). Consequently, the two identified ultramafic groups are now considered as two cumulate suites.

Amphibolite samples have basaltic to basaltic andesite major element compositions with Mg# ranging from 38.2 to 68.1 mol.%, which cannot be used to distinguish between an intermediate cumulate and a lava. Gabbroic rocks usually display a cumulate signal, either cpx-dominated or plag-dominated, leading to a REE pattern with LREE depletion and variable Eu anomaly (e.g., Pallister and Knight 1981). Such a signature is not observed in the

USB amphibolites. Although the presence of melt-like gabbros cannot be completely ruled out, these observations, together with the alternation of amphibolites and metasediments, point to a volcanic rather than a cumulate protolith for USB amphibolites. Specifically, we interpret the protoliths of the tholeiitic amphibolites as tholeiitic basalts, the boninitic amphibolites as boninitic basalts to basaltic andesites, and the transitional amphibolites as transitional basalts.

Relationship between ultramafic cumulates and lavas

Mineralogical and geochemical features suggest that the ultramafic cumulates and the basaltic melts are cogenetic. Indeed, tholeiitic suites are characterized by extensive cpx crystallization, whereas boninitic melts are usually opx-normative, which is directly observed within the ultramafic rocks. Geochemically, the tholeiitic and boninitic samples constitute two distinct trends (Fig. 4d) that can be interpreted as differentiation trends and exhibit two distinct REE pattern types (Fig. 5). To further test the cogenetic character of the tholeiitic cumulates and tholeiitic lavas on one hand, and the boninitic cumulates and boninitic lavas on the other, we calculated the REE concentrations of the melts in equilibrium with cpx and opx in the two different cumulate series. The parental melt calculated for cpx from tholeiitic cumulates using partition coefficients from Wood and Blundy (1997) exhibits a REE pattern parallel to that observed in transitional basalts, albeit with slightly lower HREE concentrations (Fig. 12a). Such a discrepancy is probably caused by the non-primary character of the most primitive USB tholeiitic lava and could be alleviated by fractionation of olivine and/or cpx. The same approach has been applied to the transition metals using partition coefficients from Bédard (2014) and yields the same results (Electronic Supplementary Material ESM 2). Given that, the cumulative cpx, and thus the tholeiitic cumulates, represent a cumulative phase of the tholeiitic-to-transitional suite (Fig. 12a).

The calculated liquid in equilibrium with magmatic opx from boninitic ultramafic cumulates using partition coefficients of Bédard (2007) reproduces the typical U-shaped pattern observed in boninitic melts (Fig. 12b). Compared to USB boninitic amphibolites, the calculated melt has a pronounced REE depletion. Once again, the most primitive USB boninitic melt has probably crystallized a certain amount of olivine and/or opx prior to extraction, which would explain its REE enrichment compared to the calculated REE composition. The same modeling for the transition metals results in similar compositions between the liquid in equilibrium with opx and the boninitic lavas (Electronic Supplementary

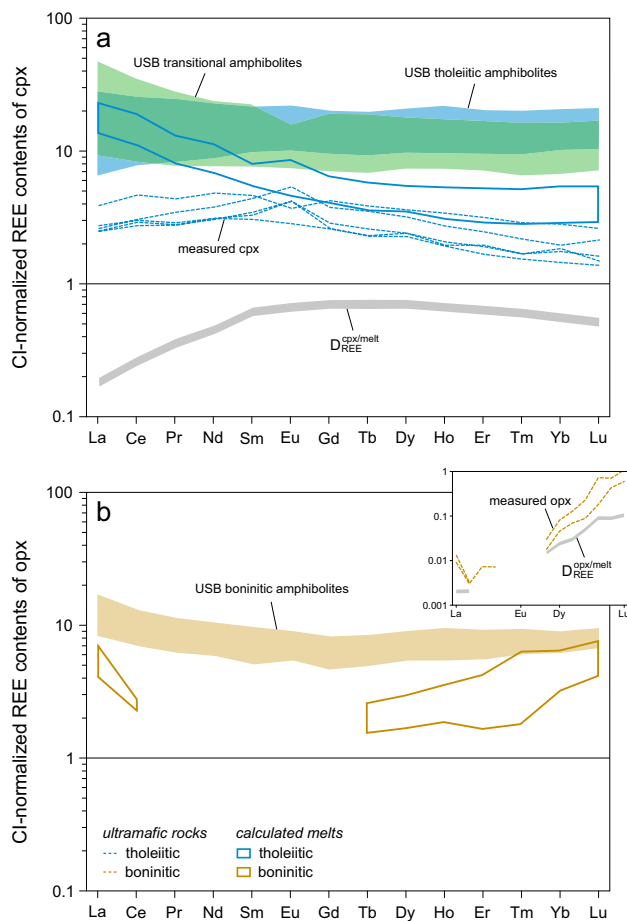


Fig. 12 Pyroxene trace element compositions and their calculated parental melts. **a** Clinopyroxene compositions from tholeiitic ultramafic rocks and the calculated melt. The partition coefficients (Wood and Blundy 1997) are calculated for pressures of 0.4–1.0 GPa and temperatures of 1150–1200 °C and are also represented. **b** Orthopyroxene compositions from boninitic ultramafic rocks, and their calculated parental melts using the partition coefficients of Bédard (2007). The top right panel of **b** shows the opx compositions used for calculation and the calculated partition coefficients. The blue, green, and brown arrays represent the USB tholeiitic, transitional, and boninitic basalts compositions. Normalization values are from Sun and McDonough (1989). Abbreviations as in the text

Material *ESM 2*). We, therefore, interpret the boninitic ultramafic rocks as cumulates of the boninitic basalts.

Primitive melts and liquid lines of descent

As previously discussed, most amphibolites from the USB have characteristics of liquids, and some of them have chemical attributes of primitive liquids that can be primary melts in equilibrium with mantle olivine with an $Mg\#$ of 87–91 mol.% and a Ni content of 1800–4500 ppm (Electronic Supplementary Material *ESM 2*). However, the REE modeling showed that these melts cannot be considered primary magmas but rather as parental melts.

This is confirmed by the calculated melt $Mg\#$ from cpx compositions, following the method described by Wood and Blundy (1997), being higher (> 75 mol.%) than $Mg\#$ from the amphibolites. The most primitive tholeiitic melt (IN14009) has $SiO_2 = 46.5$ wt.%, $MgO = 9.4$ wt.%, $Mg\# = 60$ mol.%, Ni = 394 ppm, and Cr = 356 ppm (Fig. 13). The most primitive boninitic melt (IN12034) has $SiO_2 = 50.4$ wt.%, $MgO = 12.4$ wt.%, $Mg\# = 68$ mol.%, Ni = 162 ppm, and Cr = 807 ppm (Fig. 13). These parental melts can be used to model the evolution of these two series.

Tholeiitic(-to-transitional) and boninitic liquids SiO_2 , $Mg\#$, Al_2O_3/TiO_2 , and $(Dy/Yb)_N$ variations are modeled following the method of Jagoutz (2010) using a rearrangement of the mass balance equation. The model assumes fixed cumulate compositions subtraction, although compositions may vary with fractionation, rather than mineral–liquid partition coefficients to allow major element modeling. The proportions of removed phases are adjusted to match the major and trace-element data (Fig. 13).

Tholeiitic(-to-transitional) suite

Sample IN16098b represents the only cpx-bearing ultramafic rock in our sample collection. Nevertheless, and as discussed in previous sections, the primitive parental melt probably crystallized olivine as the liquidus phase, followed by cpx leading to the formation of dunite, wehrlite and (olivine-)clinopyroxenite. This observation contrasts with the ISB cumulates sequence where no cpx has been observed nor inferred from the bulk-rock compositions (Szilas et al. 2015). Olivine and cpx fractionation induced enrichment of SiO_2 , Al_2O_3 , TiO_2 , and REE coupled with a rapid $Mg\#$ decrease and slow Al_2O_3/TiO_2 and $(Dy/Yb)_N$ decrease in the residual melt (Fig. 13). A similar evolution is observed within the crystallizing cpx. The inferred crystallization of limited amounts of plag and amph then leads to the formation of plag- and hbl-bearing pyroxenite and hbl-gabbro ($Mg\# \approx 65$ mol.%, $SiO_2 \approx 46$ wt.%) and drives the melt towards higher SiO_2 values, and to lower $Mg\#$, Al_2O_3/TiO_2 and $(Dy/Yb)_N$ values (Fig. 13). The relatively high SiO_2/MgO and Al_2O_3 contents coupled with the positive Eu anomaly of several tholeiitic cumulates corroborate the appearance of plag in the cumulate assemblage of the tholeiitic suite. The rather delayed onset of plag crystallization allows the melt to evolve towards higher SiO_2 values early during its differentiation. Finally, the most evolved andesitic compositions of the tholeiitic suite can be reproduced from a primitive melt undergoing > 60 wt.% crystallization of olivine + cpx + plag ± hbl. Such a cumulate line of descent is symptomatic of damp tholeiitic systems and is consistent with the mineral assemblage

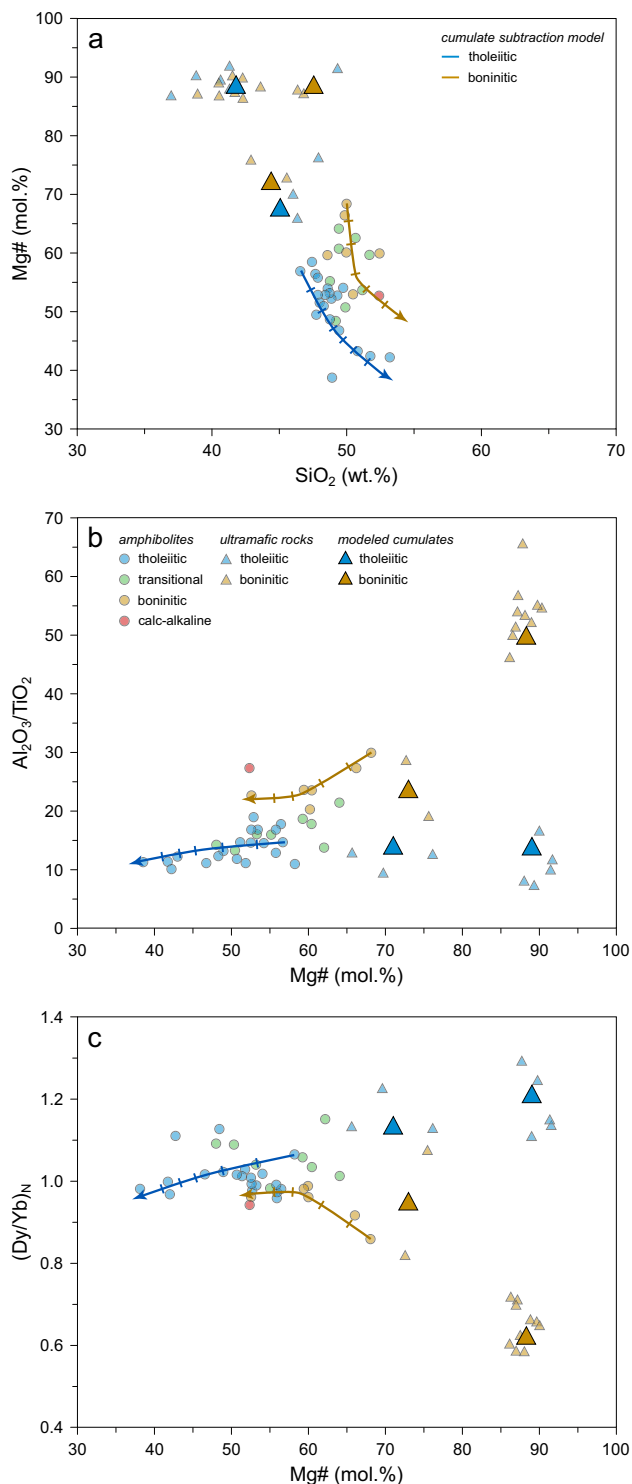


Fig. 13 Results of the fractionation models for the tholeiitic and boninitic suites. **a** SiO_2 (wt.%) vs. Mg\# (mol.%). **b** Mg\# (mol.%) vs. $\text{Al}_2\text{O}_3/\text{TiO}_2$. **c** Mg\# (mol.%) vs. $(\text{Dy}/\text{Yb})_N$. The blue and brown solid lines illustrate the liquid lines of descent of the tholeiitic and boninitic suites calculated following the model of Jagoutz (2010) based on bulk-rock cumulate subtraction. Small lines indicate a 10 wt.% fractionation step. The larger triangle symbols illustrate the fractionated cumulate compositions, and the smaller triangle symbols represent the measured USB cumulate compositions. The (most) primitive melt compositions are displayed by the start of the lines

derived from Feig et al. (2006) experiments performed at 0.5 GPa using a water-undersaturated tholeiitic magma.

Boninite-like suite

Boninitic cumulates are well represented in the collected samples, but no olivine has been observed in these samples. Nonetheless, as previously discussed, olivine probably appears as the liquidus phase. The primitive parental liquid thus probably formed dunite, websterite and orthopyroxene whose fractionation led to a rapid Mg\# (< 60 mol.%) and $\text{Al}_2\text{O}_3/\text{TiO}_2$ decrease at constant SiO_2 content ($\text{SiO}_2 \approx 50$ wt.%) in the residual liquid (Fig. 13). In addition, olivine and opx fractionation enhanced the REE, and especially the LREE, concentration in the melt resulting in a $(\text{Dy}/\text{Yb})_N$ increase (Fig. 13c). With increasing differentiation, opx become Al- and Ti-rich, reflecting the progressive enrichment of these elements in the melt. Subsequent plag and amph fractionation is documented by the gabbroic composition of the most evolved boninitic cumulates and leads to (hbl-)norite crystallization after $\sim 30\%$ fractionation, which is characteristic of silica-rich primitive melts (e.g., Grove et al. 2002). Although the exact onset of plag and hbl crystallization is uncertain, their role in the final differentiation of the boninitic melts remains limited, with a slight decrease in $\text{Al}_2\text{O}_3/\text{TiO}_2$ and $(\text{Dy}/\text{Yb})_N$. This observation agrees with the low bulk-rock SiO_2/MgO ratios of the boninitic cumulates (Fig. 11). Interestingly, the range of boninitic melt compositions is probably controlled by the composition of the primitive liquids. Indeed, some samples display SiO_2 contents ranging from 48 to 52 wt.% at a constant Mg\# of ~ 60 mol.%, which, in a differentiation sequence dominated by olivine + opx, can only be explained by primary melt compositions with a large spectrum of SiO_2 contents. Finally, boninitic melt compositions are best explained by 40–50 wt.% fractionation of subsequent olivine + opx \pm plag \pm amph. The experiments of Van der Laan (1989) reproduce the olivine + opx liquidus assemblage in a boninitic system at 0.3–0.4 GPa, 1200–1260 °C, and initial H_2O contents of 1.0–3.1 wt.%.

Implications for Hadean–Eoarchean geodynamics

Age and origin of the inherited Hadean component of the Innuksuac complex

We demonstrated that magmatic rocks of the USB formed following two liquid lines of descent, one from a damp basaltic primitive melt and the other from a wet boninitic primitive melt that are ubiquitous and best produced during low-pressure mantle melting in subduction systems. As shown in Fig. 14, boninitic lavas are chemically more depleted than tholeiitic lavas and carry an isotopically

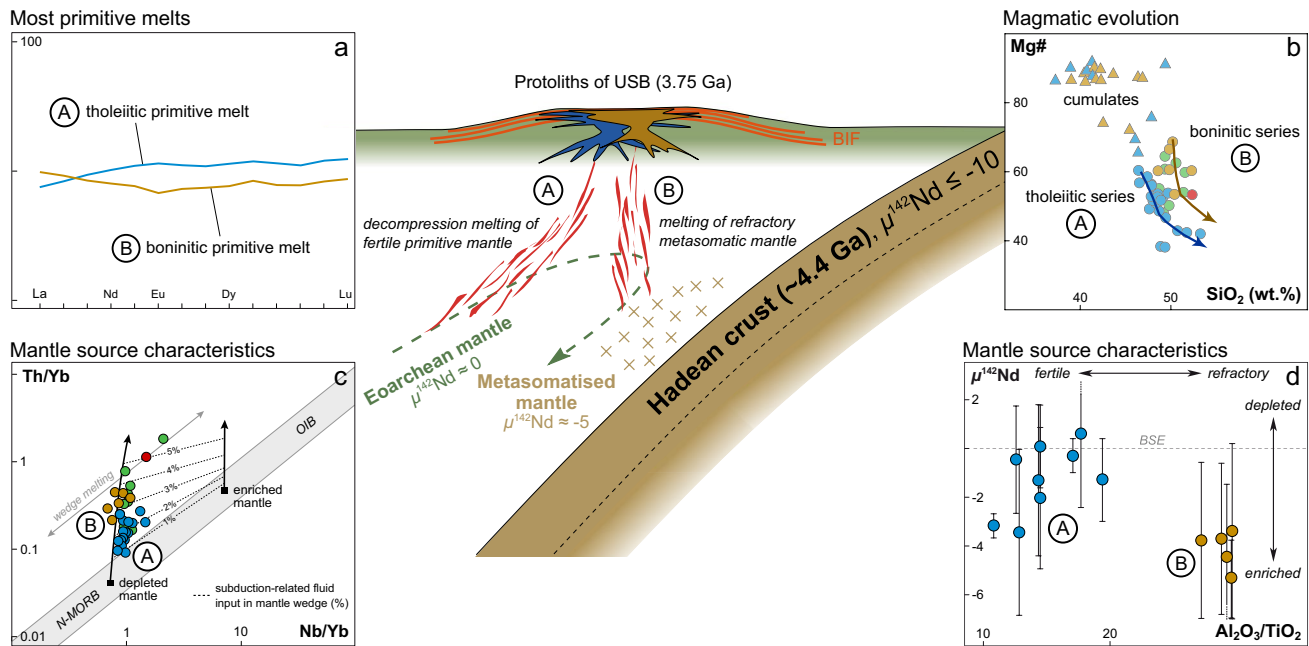


Fig. 14 Geodynamic model accounting for the petrological, geochemical, and isotopic characteristics of the Ukalik supracrustal belt. **a** Rare-earth element patterns of tholeiitic and boninitic (most) primitive melts. The boninite-like primitive melt display a U-shaped REE pattern and is more depleted than the tholeiitic primitive melt, consistent with a refractory mantle source and the absence of crustal assimilation. **b** SiO_2 (wt.%) vs. Mg# (mol.%) diagram highlighting the magmatic evolution of the Ukalik melts. **c** Th/Yb vs. Nb/Yb diagram from Pearce (2008). The metasomatic and melting vectors are from Pearce (2008). The OIB–MORB array is defined from modern mid-ocean ridges and ocean islands data. The dashed isopleths

show equal amounts of slab-derived components added to the mantle sources. Note that USB samples define a trend from the N-MORB (depleted) component to higher Th/Yb values corresponding to > 5% addition of slab-derived material. **d** $\text{Al}_2\text{O}_3/\text{TiO}_2$ vs. $\mu^{142}\text{Nd}$ (Caro et al. 2017). The tholeiitic lavas display low $\text{Al}_2\text{O}_3/\text{TiO}_2$ ratios and $\mu^{142}\text{Nd}$ contents similar to BSE, suggesting a relatively fertile, non-contaminated mantle source. In contrast, the boninitic basalts have high- $\text{Al}_2\text{O}_3/\text{TiO}_2$ ratios and lower $\mu^{142}\text{Nd}$ contents resulting from the remelting of a more depleted and metasomatized mantle source. Legend as in previous figures

enriched isotopic signature ($\mu^{142}\text{Nd} \approx -5$), while tholeiitic lavas have $\mu^{142}\text{Nd}$ values within error of the modern mantle (Fig. 14d). Previous studies also showed that $^{142}\text{Nd}/^{144}\text{Nd}$ and Sm/Nd ratios measured in the diverse amphibolite groups of the NSB and USB are positively correlated, reflecting either a mixing or an isochronous relationship (O’Neil et al. 2008; Roth et al. 2013; Caro et al. 2017). However, our results show that the $\mu^{142}\text{Nd}$ –Sm/Nd array is defined by at least two non-cogenetic series which, considered separately, have homogeneous $\mu^{142}\text{Nd}$ regardless of their Sm/Nd ratio (Caro et al. 2017). Chemical sediments (BIFs) interleaved within the Ukalik and Nuvvuagittuq mafic–ultramafic sequences also have homogeneous $\mu^{142}\text{Nd}$ despite a wide range in Sm/Nd, which conflicts with a Hadean deposition age. These observations suggest that the $\mu^{142}\text{Nd}$ –Sm/Nd array reflects contamination of Eoarchean mantle domains or mantle-derived melts by a Hadean crustal component. The differentiation age of this Hadean reservoir cannot be derived from the slope of the $\mu^{142}\text{Nd}$ –Sm/Nd array but can be estimated at ~4.4 Ga using coupled $^{146,147}\text{Sm}$ – $^{142,143}\text{Nd}$ chronometry (Caro et al. 2017). This result demonstrates that the presence of

negative ^{142}Nd anomalies coupled with LREE enrichment in amphibolites of the Innuisuc complex reflects geochemical inheritance from a crustal reservoir differentiated during or shortly after crystallization of the terrestrial magma ocean (Morino et al. 2017, 2018).

The presence of unradiogenic $^{142,143}\text{Nd}$ signatures in boninitic lavas may thus result from direct assimilation of 4.4 Ga crust by tholeiitic melts or from melting of a metasomatized mantle source triggered by the recycling of Hadean lithosphere into the mantle. As shown in Fig. 14a, boninitic melts are more depleted in incompatible elements than tholeiitic melts, which rules out a simple crustal assimilation scenario. Their hydrous character, typified by high Th, LREE, and Th/Yb (0.2–2.0) contents at constant Nb/Yb (1–2) provide further evidence in favor of fluid-induced melting of chemically depleted mantle domains (Fig. 14c). These combined petrological, geochemical, and isotopic observations suggest that tholeiitic melts were produced by decompression melting of near-primitive mantle domains. In contrast, melts displaying boninitic affinities were extracted from a more refractory mantle overprinted by a LREE-enriched fluid component carrying a crustal $^{142,143}\text{Nd}$ signature.

As mentioned in the bulk-rock chemistry section, our collection includes a unique sample (IN12032) characterized by a marked LREE enrichment and a strongly negative $\mu^{142}\text{Nd}$. Given the low solubility of Nd in aqueous fluids (Brenan et al. 1995), these features are unlikely to result solely from fluid fluxing and point towards the addition of an enriched silicate melt component to the USB mantle source. In modern arc settings, the unradiogenic ^{143}Nd - and LREE-enriched compositions of calc-alkaline lavas result primarily from partial melting of subducted sediments in the mantle wedge (e.g., Class et al. 2000; Yogodzinski et al. 2010). This stems from the fact that subducted sediments have unradiogenic $^{143}\text{Nd}/^{144}\text{Nd}$ values that contrast with the radiogenic composition of the depleted mantle (e.g., Plank and Langmuir 1998). In contrast, the oceanic crust is isotopically similar to the depleted mantle and has a low propensity to melt during subduction. As shown by Class et al. (2000) in the context of the Aleutian arc, partial melting of recycled sediments produces correlated $\text{Th}/\text{Nd}-\epsilon^{143}\text{Nd}$ variations in arc lavas, which are similar to the $\text{Th}/\text{La}-\mu^{142}\text{Nd}$ array reported by Caro et al. (2017) in USB amphibolites. The recycling of Hadean sediments may, therefore, provide a plausible mechanism for transferring unradiogenic $^{142,143}\text{Nd}$ - and LREE-enriched signatures to the mantle source of Ukaliq and Nuvvuagittuq calc-alkaline lavas. This scenario would imply accumulation of erosion products of ~ 4.4 Ga protocontinents on the Hadean seafloor and the development of differentiated felsic crust shortly after magma ocean crystallization. Alternatively, higher lithospheric buoyancy may have favored long-term preservation of Earth's primordial lithosphere (e.g., Korenaga 2006), allowing the development of unradiogenic $^{142,143}\text{Nd}$ compositions even in a predominantly mafic crustal reservoir. The elevated temperature of the Eoarchean mantle would then provide the necessary conditions for partial melting of this recycled Hadean crust and the production of high Th/La - and LREE-enriched melts capable of generating the isotopic and trace element signature of calc-alkaline amphibolites of the Innuksuac complex.

The question of Eoarchean subduction

The petrological, geochemical, and isotopic characteristics summarized in Fig. 14 provide a unique view of a magmatic system associated with the recycling of the Hadean lithosphere in the mantle. The petrogenetic history inferred from these observations can, therefore, shed some light on Eoarchean geodynamics, which otherwise strongly rely on thermomechanical and analog modeling studies (e.g., Sizova et al. 2010; Fischer and Gerya 2016a, b; Van Hunen and Van den Berg 2008; Piccolo et al. 2019). Based on these models, two contrasting views are provided, nevertheless supported by the incomplete geological record of the Archean Earth (e.g., Bédard 2018; Van Kranendonk 2010). They are: (i)

the active-lid model, in which crustal recycling occurs by subduction (e.g., Fischer and Gerya 2016b; Van Hunen and Moyen 2012); and (ii) the stagnant-lid model, where crustal recycling proceeds via dripping of eclogitized lower crust (e.g., Fischer and Gerya 2016a; Moore and Webb 2013; Piccolo et al. 2019). These processes are not mutually exclusive, and transitional regimes involving episodic or plume-induced subduction in a predominantly stagnant-lid regime have also been suggested for the Archean Earth (e.g., O'Neill et al. 2007; Gerya et al. 2015). In the subduction model, slab-induced corner flow leads to H_2O -assisted decompression melting, generating tholeiitic melts. Harzburgitic residue can further melt in a forearc position at low pressure in fluid-saturated conditions to yield boninitic melts (Grove et al. 2002; Schmidt and Jagoutz 2017). These two melting regimes can be juxtaposed in a forearc sequence and are thought to represent subduction initiation (see Stern et al. 2012), as was proposed for the nearby Nuvvuagittuq supracrustal belt (Turner et al. 2014). In the stagnant-lid model, the dripping of hydrothermally altered mafic crust induces the production of TTG-like melts and recycling of refractory eclogitic residues in the mantle (Piccolo et al. 2019). Asthenospheric uplift triggered by lower crustal dripping can, in turn, produce tholeiitic melts by decompression melting. Although recycled eclogitic residues are expected to be relatively dry, providing limited opportunity for further dehydration and fluid-induced melting of the mantle, hydrated material may be dragged along lower crustal drips (Piccolo et al. 2019) and potentially create petrogenetic environments similar to those observed in subduction settings. In contrast to subduction, however, dripping would only occur due to crustal overthickening and, therefore, does not provide a direct pathway to producing low-pressure boninitic melts. Lower crustal dripping would also favor hybridization of newly formed TTG and tholeiitic melts with preexisting (Hadean) crustal components (e.g., Fischer and Gerya 2016a; Piccolo et al. 2019), which conflicts with the lack of geochemical relationship reflecting direct assimilation of Hadean crust, and the absence of inherited Hadean zircons in the Innuksuac complex. Therefore, the most parsimonious way to explain the ubiquitous presence of Hadean geochemical crustal signatures in the absence of relict Hadean crustal components is to recycle this ancient lithosphere through subduction.

In contrast to modern arcs, the USB is dominated by tholeiitic lavas and includes only minor boninitic and calc-alkaline components. This difference may reflect the inherently short-lived nature of subduction systems in a hotter mantle, as modeled by Van Hunen and Van den Berg (2008). Alternatively, Fischer and Gerya (2016b) showed that with increasing mantle potential temperatures, magmatic activity in the mantle wedge would become dominated by decompression melting of dry asthenospheric mantle rather than

fluid-fluxed melting characterizing modern arcs. Therefore, the dominant tholeiitic and subordinate boninitic and calc-alkaline compositions of the USB may reflect the prevailing magmatic expression of subduction in a hotter mantle rather than the embryonic stages of arc development. Going beyond these different scenarios, our results suggest that subduction systems were operative, at least intermittently, as early as 3.8 Ga and thus contributed to the genesis of Earth's oldest crust. Conflicting evidence for stagnant-lid or subduction-associated tectonic processes in the Archean can be reconciled by hybrid models involving either concomitant (e.g., Gerya et al. 2015) or alternating (O'Neill et al. 2007) plume and subduction-induced magmatism.

Conclusions

The Eoarchean (ca. 3.78–3.75 Ga) Ukaliq supracrustal belt is part of the Innuksuac complex within the ca. 12,000 km² Inukjuak domain (Québec, Canada). The Ukaliq supracrustals host mafic and ultramafic rocks which can be subdivided into five categories according to their phase relationships and bulk-rock chemistry: (i) tholeiitic basalts; (ii) boninitic basalts to andesites exhibiting TiO₂ depletion and U-shaped REE pattern; (iii) transitional basalts representing a continuum between the two categories above; (iv) cpx-bearing, tholeiitic(-to-transitional) cumulates; and (v) cpx-absent, boninitic cumulates. We show through bulk-rock and mineral analyses coupled with melt composition calculations that the ultramafic rocks represent cumulate products of the mafic lavas and used these data to model a damp tholeiitic liquid line of descent consisting of olivine + cpx + plag ± hbl fractionation, and a wet boninitic differentiation sequence that crystallized olivine + opx ± plag ± hbl. The liquid lines of descent inferred from both bulk-rock and mineral chemistry suggest that the Eoarchean Ukaliq supracrustal belt originated in an environment capable of reproducing today's subduction zone petrological processes. Such environment produces covariation between ¹⁴²Nd/¹⁴⁴Nd and Sm/Nd ratios in amphibolites of the Innuksuac complex through intake of a ¹⁴²Nd anomaly-bearing Hadean slab that imprinted the mantle wedge and its melt derivatives via fluids and/or melts carrying the ^{142,143}Nd- and HFSE-depleted and LREE-enriched signatures. This suite of interpretations would not be possible without the identification of primary magmatic signatures preserved in the Eoarchean rocks of the Ukaliq locality.

Supplementary Information The online version contains supplementary material available at <https://doi.org/10.1007/s00410-022-01904-x>.

Acknowledgements We would like to thank M. Carroll (Pituvik Landholding Corporation, Québec) for permissions for fieldwork and sample

collection. The ideas contained herein were clarified by discussions and debates with W. Bleeker, J. O'Neil, R. Carlson, and D. Francis. We thank P. Morino, N. Cates, E. Bell, F. Thibon, S. Davey, M. Guitreau, J. Oulton, A. Roth, and D. Trail for assistance in the fieldwork, and O. Müntener and A. Bénard for fruitful discussions during the writing of this paper. The paper benefited from reviews by J. Pearce and K. Szilas that greatly improved the manuscript and from editorial handling by T.L. Grove.

Funding Open access funding provided by University of Lausanne. Funding for this project was provided by the Programme National de Planétologie of CNRS/INSU and the Agence Nationale de la Recherche (Grant ANR-11-JS56-0012) to G. Caro, and by OTELO (Grant JC/2018) to P. Bouilhol. S. J. Mojzsis acknowledges funding from the Collaborative for Research in Origins (CRiO) and The John Templeton Foundation (Principal investigator: S. Benner/FfAME/Award #54466), as well as the NASA Exobiology Program (Grant 09-EXOB09-0123, NNH09ZDA001N-EXOB Investigating the Hadean Earth).

Data availability Datasets for this research are included in the Electronic Supplementary Material.

Declarations

Conflict of interest The authors declare that they have no known competing interests that could have appeared to influence the work reported in this paper.

Open Access This article is licensed under a Creative Commons Attribution 4.0 International License, which permits use, sharing, adaptation, distribution and reproduction in any medium or format, as long as you give appropriate credit to the original author(s) and the source, provide a link to the Creative Commons licence, and indicate if changes were made. The images or other third party material in this article are included in the article's Creative Commons licence, unless indicated otherwise in a credit line to the material. If material is not included in the article's Creative Commons licence and your intended use is not permitted by statutory regulation or exceeds the permitted use, you will need to obtain permission directly from the copyright holder. To view a copy of this licence, visit <http://creativecommons.org/licenses/by/4.0/>.

References

- Adam J, Green T (2006) Trace element partitioning between mica- and amphibole-bearing garnet lherzolite and hydrous basanitic melt: 1. Experimental results and the investigation of controls on partitioning behaviour. *Contrib Miner Pet* 152:1–17
- Armstrong JT (1995) CITZAF—A package of correction programs for the quantitative electron microbeam X-ray analysis of thick polish materials, thin-films, and particles. *Microbeam Anal* 4:177–200
- Barnes SJ, Roeder PL (2001) The range of spinel compositions in terrestrial mafic and ultramafic rocks. *J Pet* 42:2279–2302. <https://doi.org/10.1093/petrology/42.12.2279>
- Barnes SJ, Van Kranendonk MJ (2014) Archean andesites in the east Yilgarn craton, Australia: Products of plume-crust interaction? *Lithosphere* 6:80–92. <https://doi.org/10.1130/L356.1>
- Bédard JH (2006) A catalytic delamination-driven model for coupled genesis of Archaean crust and sub-continental lithospheric mantle. *Geochim Cosmochim Acta* 70:1188–1214. <https://doi.org/10.1016/j.gca.2005.11.008>

- Bédard JH (2007) Trace element partitioning coefficients between silicate melts and orthopyroxene: parameterizations of D variations. *Chem Geol* 244:263–303. <https://doi.org/10.1016/j.chemgeo.2007.06.019>
- Bédard JH (2014) Parameterizations of calcic clinopyroxene–melt trace element partition coefficients. *Geochem Geophys Geosyst* 15:303–336. <https://doi.org/10.1002/2013GC005112>
- Bédard JH (2018) Stagnant lids and mantle overturns: implications for Archaean tectonics, magmagenesis, crustal growth, mantle evolution, and the start of plate tectonics. *Geosci Front* 9:19–49. <https://doi.org/10.1016/j.gsf.2017.01.005>
- Bédard JH, Brouillette P, Madore L, Berclaz A (2003) Archaean cratonization and deformation in the northern Superior Province, Canada: an evaluation of plate tectonic versus vertical tectonic models. *Precambrian Res* 127:61–87. [https://doi.org/10.1016/S0301-9268\(03\)00181-5](https://doi.org/10.1016/S0301-9268(03)00181-5)
- Belousova EA, Kostitsyn YA, Griffin WL, Begg GC, O'Reilly SY, Pearson NJ (2010) The growth of the continental crust: constraints from zircon Hf-isotope data. *Lithos* 119:457–466. <https://doi.org/10.1016/j.lithos.2010.07.024>
- Bénard A, Le Losq C, Nebel O, Arculus RJ (2018) Low-Ca boninite formation by second-stage melting of spinel harzburgite residues at mature subduction zones: New evidence from veined mantle xenoliths from the West Bismarck Arc. *Contrib Miner Pet* 173:105. <https://doi.org/10.1007/s00410-018-1526-6>
- Bodinier JL, Godard M (2014) Orogenic, ophiolitic, and abyssal peridotites. *Treatise on Geochemistry*. Elsevier, Amsterdam, pp 1–73. <https://doi.org/10.1016/B0-08-043751-6/02004-1>
- Bouilhol P, Burg JP, Bodinier JL, Schmidt MW, Dawood H, Hussain S (2009) Magma and fluid percolation in arc to forearc mantle: evidence from Sapat (Kohistan, Northern Pakistan). *Lithos* 107:17–37. <https://doi.org/10.1016/j.lithos.2008.07.004>
- Bouilhol P, Schmidt MW, Burg JP (2015) Magma transfer and evolution in channels within the arc crust: The pyroxenitic feeder pipes of Sapat (Kohistan, Pakistan). *J Pet* 56:1309–1342. <https://doi.org/10.1093/petrology/egv037>
- Brenan JM, Shaw HF, Ryerson FJ, Phinney DL (1995) Mineral-aqueous fluid partitioning of trace elements at 900 °C and 2.0 GPa: Constraints on the trace element chemistry of mantle and deep crustal fluids. *Geochim Cosmochim Acta* 59:3331–3350. [https://doi.org/10.1016/0016-7037\(95\)00215-L](https://doi.org/10.1016/0016-7037(95)00215-L)
- Brey GP, Köhler T (1990) Geothermobarometry in four-phase lherzolites II. New thermobarometers, and practical assessment of existing thermobarometers. *J Pet* 31:1353–1378. <https://doi.org/10.1093/petrology/31.6.1353>
- Campbell IH (1968) The origin of heteradcumulate and adcumulate textures in the Jimberlana Norite. *Geol Mag* 105:378–383. <https://doi.org/10.1017/S0016756800054431>
- Cann JR (1970) Rb, Sr, Y, Zr and Nb in some ocean floor basaltic rocks. *Earth Planet Sci Lett* 10:7–11. [https://doi.org/10.1016/0012-821X\(70\)90058-0](https://doi.org/10.1016/0012-821X(70)90058-0)
- Caro G (2011) Early silicate Earth differentiation. *Ann Rev Earth Planet Sci* 39:31–58. <https://doi.org/10.1146/annurev-earth-040610-133400>
- Caro G, Bourdon B, Birck JL, Moorbath S (2003) ^{146}Sm – ^{142}Nd evidence from Isua metamorphosed sediments for early differentiation of the Earth's mantle. *Nature* 423:428–432. <https://doi.org/10.1038/nature01668>
- Caro G, Morino P, Mojzsis SJ, Cates NL, Bleeker W (2017) Sluggish Hadean geodynamics: Evidence from coupled $^{146,147}\text{Sm}$ – $^{142,143}\text{Nd}$ systematics in Eoarchean supracrustal rocks of the Inukjuak domain (Québec). *Earth Planet Sci Lett* 457:23–37. <https://doi.org/10.1016/j.epsl.2016.09.051>
- Cates NL, Mojzsis SJ (2007) Pre-3750 Ma supracrustal rocks from the Nuvvuagittuq supracrustal belt, northern Québec. *Earth Planet Sci Lett* 255:9–21. <https://doi.org/10.1016/j.epsl.2006.11.034>
- Cates NL, Mojzsis SJ (2009) Metamorphic zircon, trace elements and Neoproterozoic metamorphism in the ca. 3.75 Ga Nuvvuagittuq supracrustal belt, Québec (Canada). *Chem Geol* 261:99–114. <https://doi.org/10.1016/j.chemgeo.2009.01.023>
- Cates NL, Ziegler K, Schmitt AK, Mojzsis SJ (2013) Reduced, reused and recycled: Detrital zircons define a maximum age for the Eoarchean (ca. 3750–3780) Nuvvuagittuq supracrustal belt, Québec (Canada). *Earth Planet Sci Lett* 362:283–293. <https://doi.org/10.1016/j.epsl.2012.11.054>
- Cawood PA, Kroner A, Pisarevsky S (2006) Precambrian plate tectonics: Criteria and evidence. *Geol Soc Am Bull* 16:4–11
- Cawood PA, Hawkesworth CJ, Dhuime B (2013) The continental record and the generation of continental crust. *Geol Soc Am Bull* 125:14–32. <https://doi.org/10.1130/B30722.1>
- Cherniak DJ, Liang Y (2012) Ti diffusion in natural pyroxene. *Geochim Cosmochim Acta* 98:31–47. <https://doi.org/10.1016/j.gca.2012.09.021>
- Chowdhury W, Trail D, Guitreau M, Bell EA, Buettner J, Mojzsis SJ (2020) Geochemical and textural investigation of the Eoarchean Ukaliq supracrustals, Northern Québec (Canada). *Lithos* 372:1–20. <https://doi.org/10.1016/j.lithos.2020.105673>
- Class C, Miller DM, Goldstein SL, Langmuir CH (2000) Distinguishing melt and fluid subduction components in Umnak Volcanics, Aleutian Arc. *Geochem Geophys Geosyst* 1:1–28. <https://doi.org/10.1029/1999GC000010>
- Connolly JAD (2005) Computation of phase equilibria by linear programming: a tool for geodynamic modeling and its application to subduction zone decarbonation. *Earth Planet Sci Lett* 236:524–541. <https://doi.org/10.1016/j.epsl.2005.04.033>
- Cooper GF, Davidson JP, Blundy JD (2016) Plutonic xenoliths from Martinique, Lesser Antilles: evidence for open system processes and reactive melt flow in island arc crust. *Contrib Miner Pet* 171:87. <https://doi.org/10.1007/s00410-016-1299-8>
- Darling JR, Moser DE, Heaman LM, Davis WJ, O'Neil J, Carlson R (2013) Eoarchean to Neoproterozoic evolution of the Nuvvuagittuq supracrustal belt: new insights from U-Pb zircon geochronology. *Am J Sci* 313:844–876. <https://doi.org/10.2475/09.2013.02>
- David J, Parent M, Stevenson R, Nadeau P, Godin L (2002) La séquence supracrustale de Porpoise Cove, région d'Inukjuak; Un exemple unique de croûte paléo-archéenne (ca. 3.8 Ga) dans la Province du Supérieur. *Ministère des Ressources naturelles et de la Faune, Québec*, pp 10–17
- Davies GF (1992) On the emergence of plate tectonics. *Geology* 20:963–966. [https://doi.org/10.1130/0091-7613\(1992\)020%3c0963:OTEOPT%3e2.3.CO;2](https://doi.org/10.1130/0091-7613(1992)020%3c0963:OTEOPT%3e2.3.CO;2)
- Deng Z, Chaussidon M, Guitreau M, Puchtel IS, Dauphas N, Moynier F (2019) An oceanic subduction origin for Archaean granitoids revealed by silicon isotopes. *Nat Geosci* 12:774–778. <https://doi.org/10.1038/s41561-019-0407-6>
- Feig ST, Koepke J, Snow JE (2006) Effect of water on tholeiitic basalt phase equilibria: an experimental study under oxidizing conditions. *Contrib Miner Pet* 152:611–638. <https://doi.org/10.1007/s00410-006-0123-2>
- Ferry JT, Spear FS (1978) Experimental calibration of the partitioning of Fe and Mg between biotite and garnet. *Contrib Miner Pet* 66:113–117. <https://doi.org/10.1007/BF00372150>
- Fischer R, Gerya T (2016a) Early Earth plume-lid tectonics: a high-resolution 3D numerical modelling approach. *J Geodyn* 100:198–214. <https://doi.org/10.1016/j.jog.2016.03.004>
- Fischer R, Gerya T (2016b) Regimes of subduction and lithospheric dynamics in the Precambrian: 3D thermomechanical modelling. *Gondwana Res* 37:53–70. <https://doi.org/10.1016/j.gr.2016.06.002>

- Fraser G, Ellis D, Eggins S (1997) Zirconium abundance in granulite-facies minerals, with implications for zircon geochronology in high-grade rocks. *Geology* 25:607–610. [https://doi.org/10.1130/0091-7613\(1997\)025%3c0607:ZAIGFM%3e2.3.CO;2](https://doi.org/10.1130/0091-7613(1997)025%3c0607:ZAIGFM%3e2.3.CO;2)
- Gale A, Dalton CA, Langmuir CH, Su Y, Schilling JG (2013) The mean composition of ocean ridge basalts. *Geochem Geophys Geosyst* 14:489–518. <https://doi.org/10.1029/2012GC004334>
- Ganguly J, Ito M, Zhang X (2007) Cr diffusion in orthopyroxene: Experimental determination, ^{53}Mn – ^{53}Cr thermochronology, and planetary applications. *Geochim Cosmochim Acta* 71:3915–3925. <https://doi.org/10.1016/j.gca.2007.05.023>
- Georoc (2021) Geochemistry of rocks of the oceans and continents. Max Planck Institute for chemistry. <http://georoc.mpch-mainz.gwdg.de/georoc/>. Accessed 24 Nov 2021
- Gerya TV, Stern RJ, Baes M, Sobolev SV, Whattam SA (2015) Plate tectonics on the Earth triggered by plume-induced subduction initiation. *Nature* 527:221–225. <https://doi.org/10.1038/nature15752>
- Greene AR, DeBari SM, Kelemen PB, Blusztajn J, Clift PD (2006) A detailed geochemical study of island arc crust: the Talkeetna arc section, South-Central Alaska. *J Pet* 47:1051–1093. <https://doi.org/10.1093/petrology/egl002>
- Greer J, Caro G, Cates NL, Tropper P, Bleeker W, Kelly NM, Mojzsis SJ (2020) Widespread poly-metamorphosed Archean granitoid gneisses and supracrustal enclaves of the southern Inukjuak Domain, Québec (Canada). *Lithos* 364:1–19. <https://doi.org/10.1016/j.lithos.2020.105520>
- Grove TL, Parman SW, Bowring SA, Price RC, Baker MB (2002) The role of an H_2O -rich fluid component in the generation of primitive basaltic andesites and andesites from the Mt. Shasta region, N California. *Contrib Miner Pet* 142:375–396. <https://doi.org/10.1007/s004100100299>
- Guitreau M, Blichert-Toft J, Mojzsis SJ, Roth AS, Bourdon B (2013) A legacy of Hadean silicate differentiation inferred from Hf isotopes in Eoarchean rocks of the Nuvvuagittuq supracrustal belt (Québec, Canada). *Earth Planet Sci Lett* 362:171–181. <https://doi.org/10.1016/j.epsl.2012.11.055>
- Hacker BR, Kelemen PB, Behn MD (2011) Differentiation of the continental crust by relamination. *Earth Planet Sci Lett* 307:501–516. <https://doi.org/10.1016/j.epsl.2011.05.024>
- Helmy HM, Yoshikawa M, Shibata T, Arai S, Tamura A (2008) Corona structure from arc mafic-ultramafic cumulates: The role and chemical characteristics of late-magmatic hydrous liquids. *J Miner Pet Sci* 103:333–344. <https://doi.org/10.2465/jmps.070906>
- Holland TJB, Blundy J (1994) Non-ideal interactions in calcic amphiboles and their bearing on amphibole-plagioclase thermometry. *Contrib Miner Pet* 116:433–447. <https://doi.org/10.1007/BF00310910>
- Holland TJB, Powell R (2011) An improved and extended internally consistent thermodynamic dataset for phases of petrological interest, involving a new equation of state for solids. *J Metamorph Geol* 29:333–383. <https://doi.org/10.1111/j.1525-1314.2010.00923.x>
- Hopkins MD, Harrison TM, Manning CE (2008) Low heat flow inferred from >4 Gyr zircons suggests Hadean plate boundary interactions. *Nature* 456:493–496. <https://doi.org/10.1038/nature07465>
- Hopkins MD, Harrison TM, Manning CE (2010) Constraints on Hadean geodynamics from mineral inclusions in > 4 Ga zircons. *Earth Planet Sci Lett* 298:367–376. <https://doi.org/10.1016/j.epsl.2010.08.010>
- Irvine TN (1967) Chromian spinel as a petrogenetic indicator: part 1. Theory *Can J Earth Sci* 2:648–672. <https://doi.org/10.1139/e65-046>
- Irvine TN, Baragar WRA (1971) A guide to the chemical classification of the common volcanic rocks. *Can J Earth Sci* 8:523–548. <https://doi.org/10.1139/e71-055>
- Jackson S (2008) Lamtrace data reduction software for LA-ICP-MS. In: Sylvester P (ed) *Laser ablation-ICP-MS in the earth sciences: current practices and outstanding issues*, 40th edn. Mineralogical Association of Canada Short Course Series, Quebec, pp 305–307
- Jagoutz O (2010) Construction of the granitoid crust of an island arc. Part II: a quantitative petrogenetic model. *Contrib Miner Pet* 160:359–381. <https://doi.org/10.1007/s00410-009-0482-6>
- Jagoutz O, Müntener O, Ulmer P, Pettko T, Burg JP, Dawood H, Husain S (2007) Petrology and mineral chemistry of lower crustal intrusions: the Chilas Complex, Kohistan (NW Pakistan). *J Pet* 48:1895–1953. <https://doi.org/10.1093/petrology/egm044>
- Johnson TE, Brown M, Kaus BJ, Van Tongeren JA (2014) Delamination and recycling of Archaean crust caused by gravitational instabilities. *Nat Geosci* 7:47–52. <https://doi.org/10.1038/ngeo2019>
- Klein C (2005) Some Precambrian banded iron-formations (BIFs) from around the world: Their age, geologic setting, mineralogy, metamorphism, geochemistry, and origins. *Am Miner* 90:1473–1499. <https://doi.org/10.2138/am.2005.1871>
- Korenaga J (2006) Archean geodynamics and the thermal evolution of Earth. *AGU Geophys Monogr Ser* 164:7–32. <https://doi.org/10.1029/164GM03>
- Krawczynski MJ, Grove TL, Behrens H (2012) Amphibole stability in primitive arc magmas: effects of temperature, H_2O content, and oxygen fugacity. *Contrib Miner Pet* 164:317–339. <https://doi.org/10.1007/s00410-012-0740-x>
- Leake BE (1978) Nomenclature of amphiboles. *Am Miner* 63:1023–1052
- Mauder B, Van Hunen J, Magni V, Bouilhol P (2016) Relamination of mafic subducting crust throughout Earth's history. *Earth Planet Sci Lett* 449:206–216. <https://doi.org/10.1016/j.epsl.2016.05.042>
- McCulloch MT, Bennett VC (1994) Progressive growth of the Earth's continental crust and depleted mantle: geochemical constraints. *Geochim Cosmochim Acta* 58:4717–4738. [https://doi.org/10.1016/0016-7037\(94\)90203-8](https://doi.org/10.1016/0016-7037(94)90203-8)
- McKenzie DAN, Bickle MJ (1988) The volume and composition of melt generated by extension of the lithosphere. *J Pet* 29:625–679. <https://doi.org/10.1093/petrology/29.3.625>
- Moore WB, Webb AAG (2013) Heat-pipe earth. *Nature* 501:501–505. <https://doi.org/10.1038/nature12473>
- Morino P, Caro G, Reisberg L, Schumacher A (2017) Chemical stratification in the post-magma ocean Earth inferred from coupled $^{146,147}\text{Sm}$ – $^{142,143}\text{Nd}$ systematics in ultramafic rocks of the Saglek Block (3.25–3.9 Ga; northern Labrador, Canada). *Earth Planet Sci Lett* 463:136–150. <https://doi.org/10.1016/j.epsl.2017.01.044>
- Morino P, Caro G, Reisberg L (2018) Differentiation mechanisms of the early Hadean mantle: insights from combined ^{176}Hf – $^{142,143}\text{Nd}$ signatures of Archean rocks from the Saglek Block. *Geochim Cosmochim Acta* 240:43–63. <https://doi.org/10.1016/j.gca.2018.08.026>
- Nandedkar RH, Ulmer P, Müntener O (2014) Fractional crystallization of primitive, hydrous arc magmas: an experimental study at 0.7 GPa. *Contrib Miner Pet* 167:1015. <https://doi.org/10.1007/s00410-014-1015-5>
- O'Neill C, Debaille V (2014) The evolution of Hadean-Eoarchean geodynamics. *Earth Planet Sci Lett* 406:49–58. <https://doi.org/10.1016/j.epsl.2014.08.034>
- O'Neill C, Lenardic A, Moresi L, Torsvik TH, Lee CT (2007) Episodic Precambrian subduction. *Earth Planet Sci Lett* 262:552–562. <https://doi.org/10.1016/j.epsl.2007.04.056>

- O'Neil J, Carlson RW, Francis D, Stevenson RK (2008) Neodymium-142 evidence for Hadean mafic crust. *Science* 321:1828–1831. <https://doi.org/10.1126/science.1161925>
- O'Neil J, Francis D, Carlson RW (2011) Implications of the Nuvvuagittuq Greenstone Belt for the formation of Earth's early crust. *J Pet* 52:985–1009. <https://doi.org/10.1093/petrology/egr014>
- O'Neil J, Carlson RW, Papineau D, Levine YE, Francis D (2019) The Nuvvuagittuq greenstone belt: A glimpse of Earth's earliest crust. Earth's oldest rocks, 2nd edn. Elsevier, Amsterdam, pp 349–374. <https://doi.org/10.1016/B978-0-444-63901-1.00016-2>
- Otamendi JE, Cristofolini EA, Tibaldi AM, Quevedo FI, Baliani I (2010) Petrology of mafic and ultramafic layered rocks from the Jaboncillo Valley, Sierra de Valle Fértil, Argentina: Implications for the evolution of magmas in the lower crust of the Famatinian arc. *J S Am Earth Sci* 29:685–704. <https://doi.org/10.1016/j.jsames.2009.11.001>
- Pallister JS, Knight RJ (1981) Rare-earth element geochemistry of the Samail ophiolite near Ibra, Oman. *J Geophys Res Solid Earth* 86:2673–2697. <https://doi.org/10.1029/JB086iB04p02673>
- Pearce JA (2008) Geochemical fingerprinting of oceanic basalts with applications to ophiolite classification and the search for Archean oceanic crust. *Lithos* 100:14–48. <https://doi.org/10.1016/j.lithos.2007.06.016>
- Pearce JA (2014a) Geochemical fingerprinting of the Earth's oldest rocks. *Geology* 42:175–176. <https://doi.org/10.1130/focus022014.1>
- Pearce JA (2014b) Immobile element fingerprinting of ophiolites. *Elements* 10:101–108. <https://doi.org/10.2113/gselements.10.2.101>
- Pearce JA, Reagan MK (2019) Identification, classification, and interpretation of boninites from Anthropocene to Eoarchean using Si–Mg–Ti systematics. *Geosphere* 15:1008–1037. <https://doi.org/10.1130/GES01661.1>
- Pearce JA, Robinson PT (2010) The Troodos ophiolitic complex probably formed in a subduction initiation, slab edge setting. *Gondwana Res* 18:60–81. <https://doi.org/10.1016/j.gr.2009.12.003>
- Piccolo A, Palin RM, Klaus BJ, White RW (2019) Generation of Earth's early continents from a relatively cool Archean mantle. *Geochem Geophys Geosyst* 20:1679–1697. <https://doi.org/10.1029/2018GC008079>
- Plank T, Langmuir CH (1998) The chemical composition of subducting sediment and its consequences for the crust and mantle. *Chem Geol* 145:325–394. [https://doi.org/10.1016/S0009-2541\(97\)00150-2](https://doi.org/10.1016/S0009-2541(97)00150-2)
- Polat A, Hofmann AW, Rosing MT (2002) Boninite-like volcanic rocks in the 3.7–3.8 Ga Isua greenstone belt, West Greenland: geochemical evidence for intra-oceanic subduction zone processes in the early Earth. *Chem Geol* 184:231–254. [https://doi.org/10.1016/S0009-2541\(01\)00363-1](https://doi.org/10.1016/S0009-2541(01)00363-1)
- Putirka K (2016) Amphibole thermometers and barometers for igneous systems and some implications for eruption mechanisms of felsic magmas at arc volcanoes. *Am Miner* 101:841–858. <https://doi.org/10.2138/am-2016-5506>
- Reagan MK, Ishizuka O, Stern RJ, Kelley KA, Ohara Y, Blichert-Toft J, Bloomer SH, Cash J, Fryer P, Hanan BB, Hickey-Vargas R, Ishii T, Kimura JI, Peate DW, Rowe MC, Woods M (2010) Forearc basalts and subduction initiation in the Izu-Bonin-Mariana system. *Geochem Geophys Geosyst* 11:1–17. <https://doi.org/10.1029/2009GC002871>
- Ringwood AE (1974) The petrological evolution of island arc systems: Twenty-seventh William Smith Lecture. *J Geol Soc Lond* 130:183–204. <https://doi.org/10.1144/gsjgs.130.3.0183>
- Roth AS, Bourdon B, Mojzsis SJ, Touboul M, Sprung P, Guitreau M, Blichert-Toft J (2013) Inherited ¹⁴²Nd anomalies in Eoarchean protoliths. *Earth Planet Sci Lett* 361:50–57. <https://doi.org/10.1016/j.epsl.2012.11.023>
- Schmidt MW, Jagoutz O (2017) The global systematics of primitive arc melts. *Geochem Geophys Geosyst* 18:2817–2854. <https://doi.org/10.1002/2016GC006699>
- Shirey SB, Richardson SH (2011) Start of the Wilson cycle at 3 Ga shown by diamonds from subcontinental mantle. *Science* 333:434–436. <https://doi.org/10.1126/science.1206275>
- Simard M, Parent M, David J, Sharma KNM (2003) Géologie de la région de la rivière Innuksuac (SNRC 34K et 34L). Ministère des Ressources Naturelles, Québec, pp 1–44
- Sizova E, Gerya T, Brown M, Perchuk LL (2010) Subduction styles in the Precambrian: Insight from numerical experiments. *Lithos* 116:209–229. <https://doi.org/10.1016/j.lithos.2009.05.028>
- Sleep NH (2005) Evolution of the continental lithosphere. *Annu Rev Earth Planet Sci* 33:369–393. <https://doi.org/10.1146/annurev.earth.33.092203.122643>
- Smit MA, Scherstén A, Næraa T, Emo RB, Scherer EE, Sprung P, Bleeker W, Mezger K, Maltese A, Cai Y, Rasbury ET, Whitehouse MJ (2019) Formation of Archean continental crust constrained by boron isotopes. *Geochem Perspect Lett* 12:23–26. <https://doi.org/10.7185/geochemlet.1931>
- Smithies RH, Lu Y, Kirkland CL, Johnson TE, Mole DR, Champion DC, Martin L, Jeon H, Wingate MTD, Johnson SP (2021) Oxygen isotopes trace the origins of Earth's earliest continental crust. *Nature* 592:70–75. <https://doi.org/10.1038/s41586-021-03337-1>
- Spear FS (1993) Metamorphic phase equilibria and pressure–temperature–time paths. Mineralogical Society of America Monograph, Washington
- Stern RJ (2002) Subduction zones. *Rev Geophys* 40:1–42. <https://doi.org/10.1029/2001RG000108>
- Stern RJ (2005) Evidence from ophiolites, blueschists, and ultrahigh-pressure metamorphic terranes that the modern episode of subduction tectonics began in Neoproterozoic time. *Geology* 33:557–560. <https://doi.org/10.1130/G21365.1>
- Stern RJ, Reagan M, Ishizuka O, Ohara Y, Whattam S (2012) To understand subduction initiation, study forearc crust: To understand forearc crust, study ophiolites. *Lithosphere* 4:469–483. <https://doi.org/10.1130/L183.1>
- Sun SS, McDonough WF (1989) Chemical and isotopic systematics of oceanic basalts: Implications for mantle composition and processes. *Geol Soc Spec Publ* 42:313–345. <https://doi.org/10.1144/GSL.SP.1989.042.01.19>
- Szilás K, Kelemen PB, Rosing MT (2015) The petrogenesis of ultramafic rocks in the >3.7 Ga Isua supracrustal belt, southern West Greenland: geochemical evidence for two distinct magmatic cumulate trends. *Gondwana Res* 28:565–580. <https://doi.org/10.1016/j.gr.2014.07.010>
- Taylor SR, McLennan SM (1985) The continental crust: its composition and evolution. Blackwell, Oxford
- Taylor RN, Nesbitt RW, Vidal P, Harmon RS, Auvray B, Croudace IW (1994) Mineralogy, chemistry, and genesis of the boninite series volcanics, Chichijima, Bonin Islands, Japan. *J Pet* 35:577–617. <https://doi.org/10.1093/petrology/35.3.577>
- Trail D, Boehnke P, Savage PS, Liu MC, Miller ML, Bindeman I (2018) Origin and significance of Si and O isotope heterogeneities in Phanerozoic, Archean, and Hadean zircon. *Proc Natl Acad Sci USA* 115:10287–10292. <https://doi.org/10.1073/pnas.1808335115>
- Tribuzio R, Tiepolo M, Thirlwall MF (2000) Origin of titanian pargasite in gabbroic rocks from the Northern Apennine ophiolites (Italy): insights into the late-magmatic evolution of a MOR-type intrusive sequence. *Earth Planet Sci Lett* 176:281–293. [https://doi.org/10.1016/S0012-821X\(00\)00014-5](https://doi.org/10.1016/S0012-821X(00)00014-5)
- Turner S, Rushmer T, Reagan M, Moyaen JF (2014) Heading down early on? Start of subduction on Earth. *Geology* 42:139–142. <https://doi.org/10.1130/G34886.1>

- Van der Laan SR (1989) Experimental evidence for the origin of boninites: Near-liquidus phase relations to .5 kbar. *Boninites and Related Rocks*. Unwin Hyman, London, pp 113–147
- Van Kranendonk MJ (2010) Two types of Archean continental crust: plume and plate tectonics on early Earth. *Am J Sci* 310:1187–1209. <https://doi.org/10.2475/10.2010.01>
- Van Hunen J, Moyen JF (2012) Archean subduction: fact or fiction? *Annu Rev Earth Planet Sci* 40:195–219. <https://doi.org/10.1146/annurev-earth-042711-105255>
- Van Hunen J, Van den Berg AP (2008) Plate tectonics on the early Earth: Limitations imposed by strength and buoyancy of subducted lithosphere. *Lithos* 103:217–235. <https://doi.org/10.1016/j.lithos.2007.09.016>
- Van Thienen P, Van den Berg AP, Vlaar NJ (2004) Production and recycling of oceanic crust in the early earth. *Tectonophysics* 386:41–65. <https://doi.org/10.1016/j.tecto.2004.04.027>
- Villiger S, Ulmer P, Müntener O (2007) Equilibrium and fractional crystallization experiments at 0.7 GPa; the effect of pressure on phase relations and liquid compositions of tholeiitic magmas. *J Pet* 48:159–184. <https://doi.org/10.1093/petrology/egl058>
- Von Huene R, Scholl DW (1991) Observations at convergent margins concerning sediment subduction, subduction erosion, and the growth of continental crust. *Rev Geophys* 29:279–316. <https://doi.org/10.1029/91RG00969>
- Walker BA Jr, Bergantz GW, Otamendi JE, Ducea MN, Cristofolini EA (2015) A MASH zone revealed: the mafic complex of the Sierra Valle Fértil. *J Pet* 56:1863–1896. <https://doi.org/10.1093/petrology/egv057>
- Weller OM, Copley A, Miller WGR, Palin RM, Dyck B (2019) The relationship between mantle potential temperature and oceanic lithosphere buoyancy. *Earth Planet Sci Lett* 518:86–99. <https://doi.org/10.1016/j.epsl.2019.05.005>
- Wood BJ, Blundy JD (1997) A predictive model for rare earth element partitioning between clinopyroxene and anhydrous silicate melt. *Contrib Miner Pet* 129:166–181. <https://doi.org/10.1007/s004100050330>
- Yogodzinski GM, Vervoort JD, Brown ST, Gerseny M (2010) Subduction controls on Hf and Nd isotopes in lavas of the Aleutian island arc. *Earth Planet Sci Lett* 300:226–238. <https://doi.org/10.1016/j.epsl.2010.09.035>
- Zerkle AL (2018) Biogeodynamics: bridging the gap between surface and deep Earth processes. *Philos Trans R Soc A* 376:1–11. <https://doi.org/10.1098/rsta.2017.0401>

Publisher's Note Springer Nature remains neutral with regard to jurisdictional claims in published maps and institutional affiliations.